Received: 26 October 2025 | Revised: 4 December 2025 | Accepted: 22 December 2025
DOI: 10.1002/inf2.70126

RESEARCH ARTICLE

Conjugation-mediated and polarity-switchable interfacial layers for fast cycling of lithium-metal batteries

Jeong-A. Lee[1] | **Haneul Kang**[1] | **Yoonhan Cho**[2] | **Seong Hyeon Kweon**[3] | **Seonghyun Kim**[2] | **Syed Azkar Ul Hasan**[4] | **Minju Song**[1] | **Saehun Kim**[1] | **Eunji Kwon**[5] | **Samuel Seo**[5] | **Kyoung Han Ryu**[5] | **Rama K. Vasudevan**[6] | **Sang Kyu Kwak**[4] | **Seungbum Hong**[2] | **Nam-Soon Choi**[1]

[1]Department of Chemical and Biomolecular Engineering, Korea Advanced Institute of Science and Technology (KAIST), Daejeon, Republic of Korea
[2]Department of Materials Science and Engineering, Korea Advanced Institute of Science and Technology (KAIST), Daejeon, Republic of Korea
[3]School of Energy and Chemical Engineering, Ulsan National Institute of Science and Technology (UNIST), Ulsan, Republic of Korea
[4]Department of Chemical and Biological Engineering, Korea University, Seoul, Republic of Korea
[5]Hyundai Motor Company, Uiwang-si, Republic of Korea
[6]Center for Nanophase Materials Sciences, Oak Ridge National Laboratory (ORNL), Oak Ridge, Tennessee, USA

Correspondence
Sang Kyu Kwak, Department of Chemical and Biological Engineering, Korea University, 145 Anam-ro, Seongbuk-gu, Seoul, 02841, Republic of Korea.
Email: skkwak@korea.ac.kr

Seungbum Hong, Department of Materials Science and Engineering, Korea Advanced Institute of Science and Technology (KAIST), 291 Daehak-ro, Yuseong-gu, Daejeon 34141, Republic of Korea.
Email: seungbum@kaist.ac.kr

Nam-Soon Choi, Department of Chemical and Biomolecular Engineering, Korea Advanced Institute of Science and Technology (KAIST), 291 Daehak-ro, Yuseong-gu, Daejeon 34141, Republic of Korea.
Email: nschoi@kaist.ac.kr

Funding information
Ministry of Trade, Industry & Energy, Grant/Award Number: RS-2024-00402410; Hyundai Motor Company and a National Research Foundation of Korea (NRF), Korean Government (MSIT), Grant/Award Number: RS-2025-00554246; Korea Institute of Energy Technology Evaluation and Planning (KETEP); Center

Abstract

The solid electrolyte interphase (SEI) is a key property of lithium-metal batteries (LMBs), affecting their Coulombic efficiency, rate capability, and cycle life. However, conventional SEIs, primarily formed by the decomposition of lithium salts and fluorinated additives to create inorganic-dominant interphases, suffer from inhomogeneous Li deposition and low ionic conductivity. These intrinsic drawbacks accelerate severe side reactions with the electrolyte, cause rapid capacity fading and accumulation of dead Li, and present safety concerns, particularly under elevated current density. In this study, we unravel the essential role of the SEI on the Li-metal anode in LMBs by creating a conjugation-mediated and polarity-switchable interfacial architecture. The thiophene-embedded polymer-like SEI, formed by in situ electrochemical oligomerization of thiophene, enhances Li^+ ion conductivity by coordinating with lone electron pairs in sp^2 orbitals. Concurrently, the conjugated π systems involving sp^2 hybridized C=C bonds and S atoms enable *switchable polarity of p_z orbitals*, facilitating dynamic electron-cloud redistribution during Li plating and stripping. This orbital-level adaptability accelerates Li^+ migration, suppresses dendritic growth, and stabilizes the Li-metal surface under high-current operation. This study establishes a new paradigm in orbital-engineered interfacial design in LMBs, bridging molecular-scale electronic polarization with macroscopic fast-charging stability. Furthermore, our study underscores that fine-tuning the

for Nanophase Materials Sciences; UNIST High Performance Computing (HPC) systems; Korea Institute of Science and Technology Information, Grant/Award Number: KSC-2023-CRE-0143

properties of the SEI and the cathode electrolyte interphase is key to unlocking the transformative potential of LMBs for practical applications.

KEYWORDS

cathode electrolyte interphases, electrolyte additives, fast cycling, lithium metal, nickel-rich cathodes, solid electrolyte interphases

1 | INTRODUCTION

Li metal has gained prominence as a compelling alternative to replace high-end anodes, such as graphite-Si composites, owing to its exceptional theoretical capacity (3860 mAh g^{-1}).[1–3] However, its inherently high chemical reactivity, which results in critical limitations in the cyclability and safety of Li-metal batteries (LMBs), restricts its practical implementation.[4–6] Creating a solid electrolyte interphase (SEI) with adequate mechanical robustness and ionic conductivity in LMBs is a formidable challenge.[7–9] The physically deposited SEI lacks sufficient mechanical integrity to withstand the volumetric stress during repeated Li plating and stripping.[10,11] Microcracks are thus formed in the SEI, which serve as preferential sites for inhomogeneous Li plating.[12–15] Furthermore, the low ionic conductivity of the uncontrolled SEI severely impedes ion transport efficiency, which induces sluggish Li^+ ion movement and increases resistance in LMBs. These detrimental behaviors cause irreversible capacity loss and degradation of the overall electrochemical performance of LMBs.[16–18] Under elevated C-rates, Li-metal anodes suffer from non-uniform current distribution across the SEI, forcing localized Li^+ transport through a low-ionic resistance region and accelerating dendritic Li growth.[19–21] Moreover, as the cathode areal capacity is increased to achieve high energy density, the corresponding rise in current density at the Li-metal surface further accelerates dendritic Li growth (Equation 1).[22–28]

$$\tau \sim \pi D \left(\frac{eC_0}{2J}\right)^2 \left(\frac{\mu_a + \mu_c}{\mu_a}\right)^2. \qquad (1)$$

Consequently, recent strategies have focused on designing SEIs for fast-cycling LMBs.[29–40] Nevertheless, most reported strategies focus on forming inorganic-dominant SEIs derived from Li salt and fluorinated additive decomposition. Although such interphases can enhance interfacial stability, their fast-cycling effectiveness remains largely unverified under practical conditions, as evaluations are typically conducted using LMBs with low-areal-capacity cathodes (Table S1).

Among the diverse additives, thiophene is reportedly key in cathode stabilization, as it facilitates the formation of the ionic conductive cathode electrolyte interphase (CEI). Unfortunately, previous studies related to thiophene have largely been confined to configurations with extremely low mass loading of cathodes and limited charge/discharge rates. These restrictions have hindered the practical application of fast-cycling performance in high-energy LMBs.[41–44]

Herein, through interfacial engineering incorporating the heterocyclic compound thiophene, we present groundbreaking structural tuning of the SEI and CEI architecture to enable stable cycling at high C-rates in LMBs based on a high areal capacity of 4.1 mAh cm^{-2} of the $LiNi_{0.9}Co_{0.05}Mn_{0.05}O_2$ (NCM90) cathode. In contrast to the anion-derived SEI and the polymeric SEI formed by fluoroethylene carbonate (FEC) and vinylene carbonate (VC), the thiophene-embedded polymer-like interphases achieve fast and homogeneous Li plating/stripping behavior (Figure 1A–C). The conjugated oligomer network within the thiophene motifs not only creates an electron-rich microenvironment through the conjugated π orbitals of the C═C bonds and S atoms but also enables dynamic electron-cloud rearrangement via polarity switching of p_z orbitals, which facilitates Li^+ ions attraction and promotes uniformly redistributing electrons across the Li-metal surface. This process enhances Li^+ ion transport while mitigating dendritic Li formation during cycling (Figure 1D). The repeated structure of the thiophene-embedded polymer-like interfaces collectively accelerates interfacial Li^+ ion transfer kinetics on Li-metal anodes.[45–49] Moreover, thiophene ensures sufficient interfacial stability of the NCM90 cathodes by modulating the CEI composition, thereby maintaining the structural integrity over high C-rate cycling in LMBs. Thus, this work establishes a new paradigm in orbital-engineered interfacial chemistry by introducing a conjugation-mediated and polarity-switchable interfacial architecture of thiophene-embedded polymer-like SEI. Compared with previous studies, the proposed method enables high energy-density LMBs using NCM90 cathodes with a high areal capacity of 4.1 mAh cm^{-2}, demonstrating exceptional cyclic stability under a low electrolyte/capacity (E/C) ratio of 1.5 g Ah^{-1} and a high

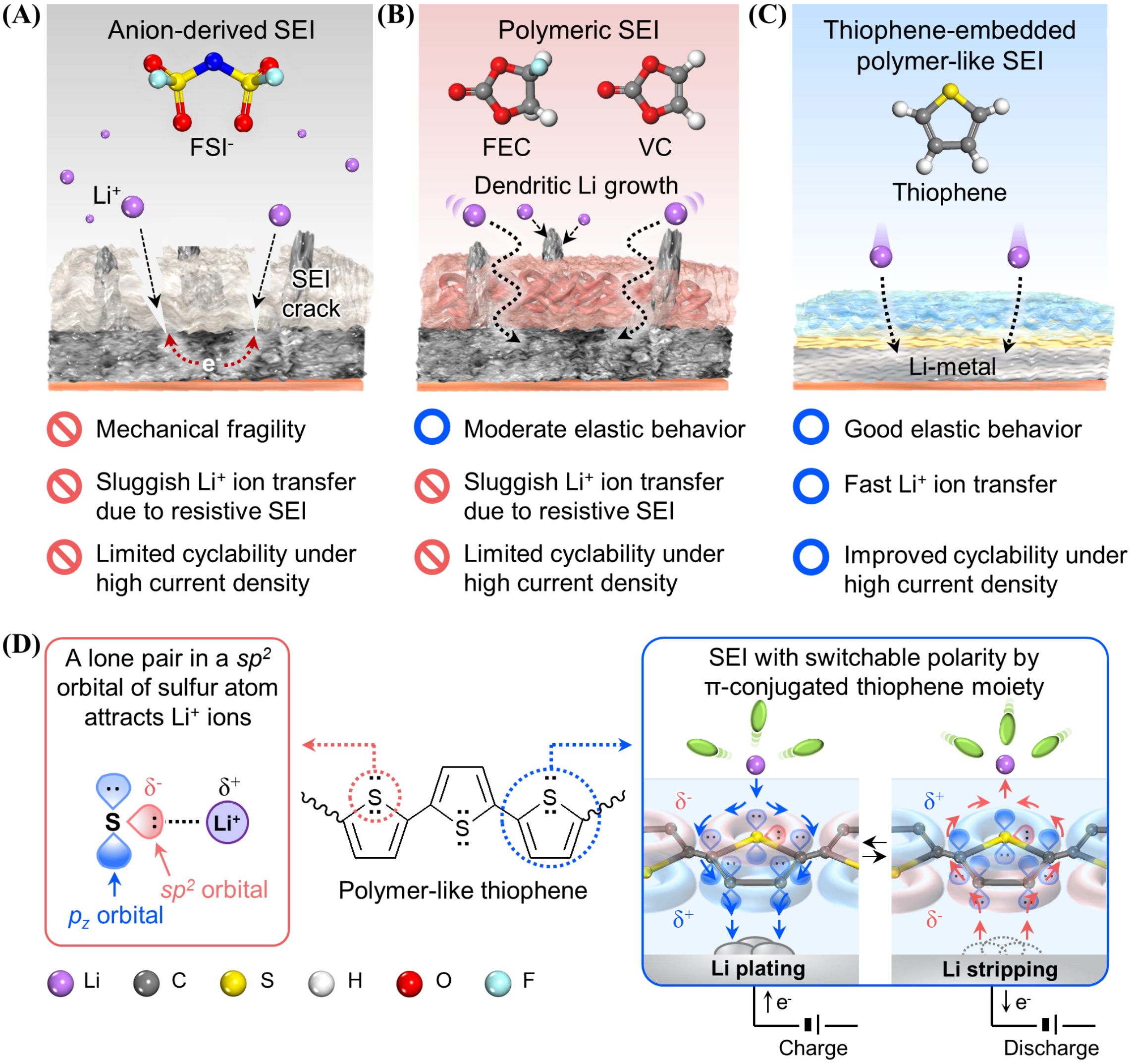

FIGURE 1 Thiophene-embedded polymer-like SEI for enabling fast cycling. Schematic of the characteristics of the (A) anion-derived SEI, (B) polymeric SEI formed by FEC or VC, and (C) thiophene-embedded polymer-like SEI. (D) Li^+ ion transfer mechanism through the thiophene-embedded polymer-like SEI during charging. EL, electrolyte; FEC, fluoroethylene carbonate; SEI, solid electrolyte interphase; VC, vinylene carbonate.

current density of 8.2 mA cm^{-2}. Furthermore, large-area pouch cell assessments were performed, demonstrating the scalability and reliable performance of the developed electrolyte system under practical conditions involving high current densities.

2 | RESULTS AND DISCUSSION

2.1 | Optimization of SEI architecture for rapid cycling in LMBs

Compared to *N,N*-dimethylsulfamoyl fluoride (FSA), containing a fluorosulfonyl functional group and having a weak solvating ability toward Li^+, 1,2-dimethoxyethane (DME) exhibited a stronger solvating ability, enabling the formation of Li^+-DME coordination complexes within the solvation sheath of 3 M lithium bis(fluorosulfonyl) imide (LiFSI) in a DME electrolyte (Figure S1). The sluggish desolvation of these complexes accelerated DME decomposition, forming an organic-dominant SEI layer on Li-metal anodes (Figures S2 and S3). By contrast, using 3 M LiFSI in FSA completely altered the interfacial engineering, facilitating the formation of robust, LiF-enriched SEI on Li-metal anodes. The baseline electrolyte—3 M LiFSI in FSA—demonstrated improved cycling stability compared with that of 3 M LiFSI in DME (denoted as 3 M DME) (Figures S4 and S5). Notably, the baseline electrolyte enabled stable Li plating/stripping with high Li^+ reversibility at low current density (Figure S6). Furthermore, FSA, which has better oxidation durability than DME, effectively suppressed oxidative electrolyte decomposition under charging-voltage conditions of 4.25 V versus Li/Li$^+$, thereby enhancing the cycle performance of Li/NCM90 full cells at a moderate C-rate of C/3 (Figures S7–S9).[50–52] However, as the cycling rate increased from C/3 to 2 C, the LiF-rich SEI impeded Li$^+$ ion transport, leading to an abrupt decrease in the discharge capacity and severe fluctuations in the Coulombic efficiency (CE) in LMBs containing the baseline electrolyte (Figure S10). According to Sand's law, Li$^+$ ion mobility, which is limited by the high-resistance SEI, may accelerate dendritic Li growth under high current densities (Equation 1).

In this regard, optimizing the interfacial structures to enhance Li$^+$ ion transport was crucial for attaining stable performance in LMBs under rapid cycling conditions with a high areal capacity of the cathodes. To construct robust electrode-electrolyte interfaces, 1 wt.% of FEC, VC, or thiophene was utilized as an additive in the baseline electrolyte, hereinafter referred to as FEC, VC, and thiophene-based electrolytes, respectively. The additive concentration was optimized through a series of electrochemical evaluations and surface characterization analyses of the Li-metal anodes, as shown in Figures S11–S16. In contrast to the other additives, thiophene, owing to its narrow energy bandgap and lower adsorption energy toward Li-metal, preferentially formed interfacial layers on both electrodes in LMBs (Figures 2A–D, S17, and S18). X-ray photoelectron spectroscopy measurements confirmed the creation of a C—S-based interfacial layer in both the Li-metal anode and NCM90 cathode, which is attributed to the electrochemical decomposition of thiophene (Figures S19 and S20). To elucidate the detailed mechanism and structure of the thiophene-driven SEI on Li-metal, density functional theory (DFT) calculations were utilized (Figure 2C). In this process, thiophene, upon accepting electrons from the Li-metal, formed a C-centered radical and underwent polymerization through interaction between thiophene radicals. Two possible dimerization pathways of C—C and C—S bonding revealed formation energies of −0.69 and 2.92 eV, respectively, indicating that polymerization is thermodynamically more favorable via C—C bond coupling. Based on these results, the polymerization reaction mechanism of thiophene radicals was further investigated (Figure 2D). A trans-binary structure (thiophene–thiophene radical) formed when one thiophene radical formed a C—C bond with another; the exothermic process suggests that higher-order polymeric structures can be generated through similar reactivity. Subsequently, the interaction between these polymeric SEIs and Li was investigated by calculating the adsorption energies of poly(FEC), poly(VC), and poly(thiophene) in the presence of Li atoms (Figure 2E–G). The calculated adsorption energies of −0.34, −0.37, and −1.43 eV, respectively, indicate that poly(thiophene) exhibits a markedly stronger affinity for Li relative to those of the other polymer networks, suggesting more efficient Li$^+$ transport in thiophene-based SEI (Figure 2H). Notably, by integrating these theoretical findings, time-of-flight secondary ion mass spectrometry (TOF-SIMS) spectra demonstrated polymerization-specific signals at $m/z = 84$, 164, and 244 on the Li-metal anode precycled in the thiophene-based electrolyte (Figure S21). By contrast, the baseline electrolyte did not display notable peaks beyond Cs. In contrast to the baseline electrolyte, which primarily formed inorganic-rich SEI via the decomposition of LiFSI and FSA solvent, the thiophene-based electrolyte underwent reductive decomposition, resulting in the creation of polymeric SEI on the outermost surface of the Li-metal anodes (Figure S22). Ex situ Raman spectroscopy further corroborated the structural characterization of the thiophene-embedded polymer-like SEI, where an airtight cell was utilized to minimize potential alterations in the SEI components caused by air exposure (Figures S23 and S24). The thiophene-embedded polymer-like SEI displayed C—C and C═C vibrational features analogous to those observed in poly(3-octylthiophene-2,5-diyl) (P_3OT), which consists of repeating thiophene units. Interfacial-property analyses and DFT computations revealed that the thiophene-embedded polymer-like SEI comprised repetitive arrangement of the thiophene motifs. In addition, Raman spectroscopy identified a characteristic trans-type C—C coupling band, consistent with DFT-predicted oligomeric structures, validating the presence of thiophene-derived conjugated oligomers within the SEI.[53–56] To extend these insights, model polymers with different repeating units were introduced into the baseline electrolyte, and Li/Li symmetric cells were used to examine interfacial resistance (Figure S25). Impedance measurements revealed that poly(propylene sulfide) offered lower resistance than poly(propylene carbonate), which comprises ester groups. Notably, P_3OT significantly reduced the interfacial resistance of Li/Li symmetric cells, underscoring the advantageous role of the thiophene-embedded polymer-like SEI in facilitating efficient Li$^+$ transfer at the Li-metal anode. Collectively, these experimental and theoretical results demonstrate the polymerization of thiophene radicals via C—C bond formation to yield a highly Li$^+$ ionic conductive SEI, thereby enhancing the interfacial kinetics and long-term stability of Li-metal anodes under rapid cycling conditions.

2.2 | Li plating and stripping behavior under high current densities

Thiophene underwent in situ electro-oligomerization during the charging process, forming multiple

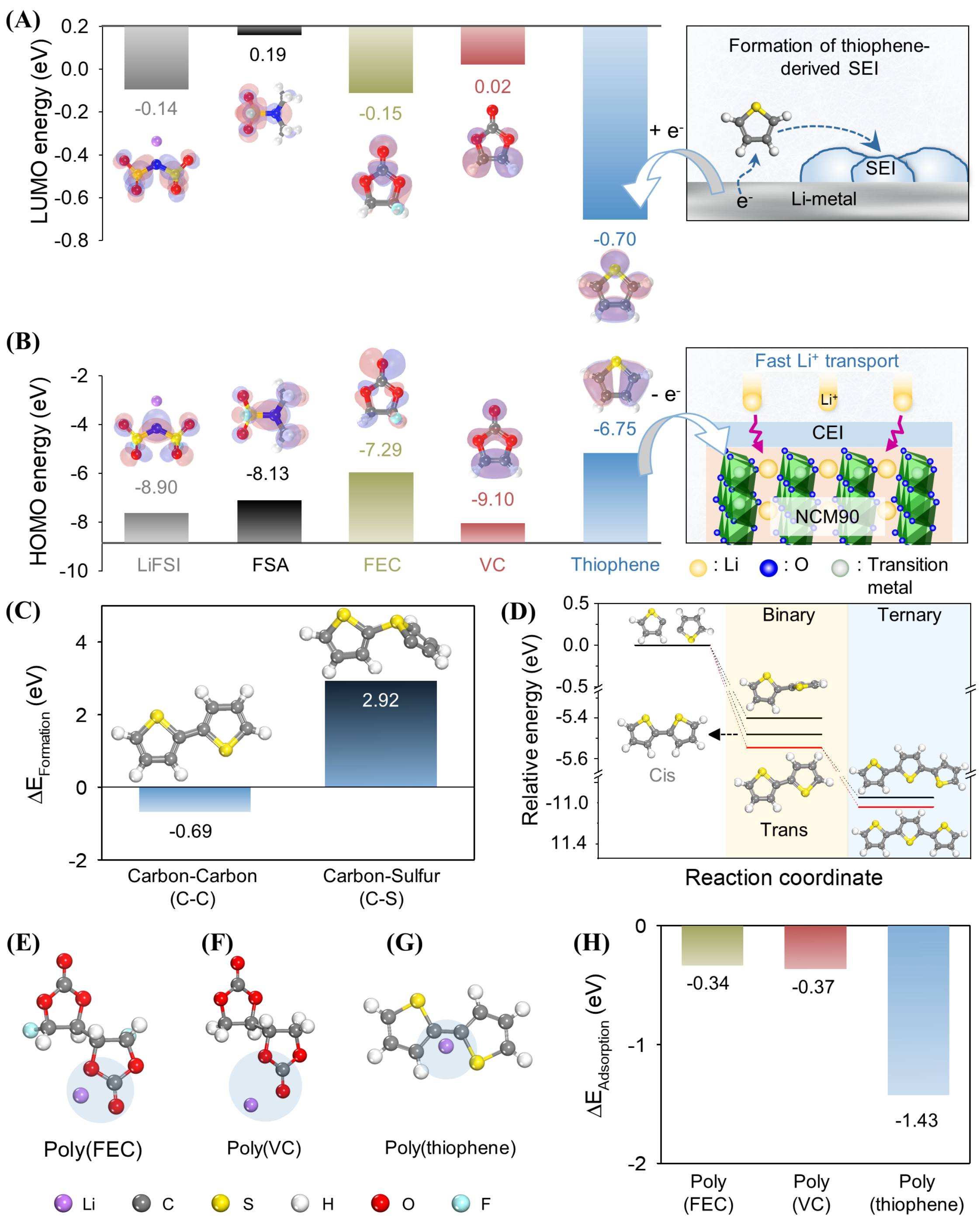

FIGURE 2 Formation principles of a thiophene-embedded polymer-like SEI on the Li-metal anode. (A) LUMO and (B) HOMO energy diagrams of LiFSI, FSA, and additives. (C) Formation energy ($\Delta E_{\text{Formation}}$) of the thiophene dimerization pathway of C—C and C—S bonding. (D) Relative energy diagram of polymeric reaction starting from thiophene radicals to ternary thiophene. Adsorption structure of the Li atom on (E) poly(FEC), (F) poly(VC), and (G) poly(thiophene). Note that adsorption sites for the Li atom are the thermodynamically most favorable. (H) Adsorption energy ($\Delta E_{\text{Adsorption}}$) of poly(FEC), poly(VC), and poly(thiophene) with a Li atom. FEC, fluoroethylene carbonate; FSA, *N*,*N*-dimethylsulfamoyl fluoride; HOMO, highest occupied molecular orbital; LiFSI, lithium bis(fluorosulfonyl)imide; LUMO, lowest unoccupied molecular orbital; SEI, solid electrolyte interphase; VC, vinylene carbonate.

thiophene-linked polymeric species (Figure S21). To validate the switchable polarity of the thiophene-embedded polymer-like SEI, orbital analysis across four representative stages of Li^+ plating/stripping process was conducted (Figure 3A). The conjugated thiophene motifs, which consisted of an electron-rich environment, promoted

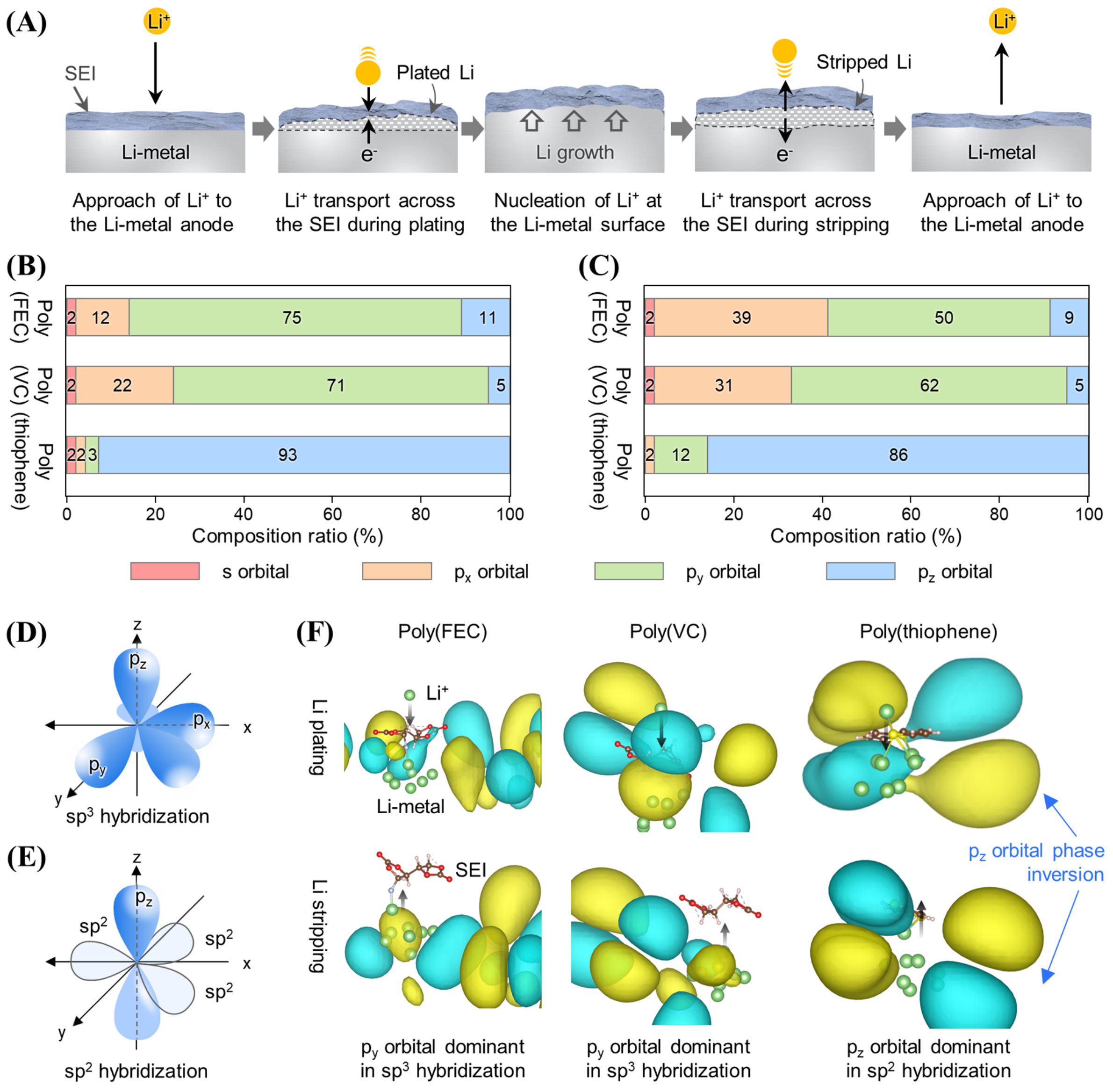

FIGURE 3 Unique characteristics of the SEI ensuring interfacial stability of the Li-metal anode under high current density. (A) Schematic of representative stages of Li plating and stripping. Orbital composition analysis of poly(FEC), poly(VC), and poly(thiophene) in (B) Li plating and (C) stripping, highlighting the contributions of frontier orbitals to Li$^+$ transport. (D) Sp^3 hybridized orbitals in poly(FEC) and poly(VC). (E) Sp^2 hybridized orbitals in poly(thiophene). (F) Dominant orbital distributions of poly(FEC), poly(VC), and poly(thiophene) in the Li plating and stripping process. Yellow and cyan lobes represent the positive and negative phases of the wave function, respectively. FEC, fluoroethylene carbonate; SEI, solid electrolyte interphase; VC, vinylene carbonate.

uniform and rapid Li$^+$ transport by enabling dynamic electron-cloud redistribution during Li plating/stripping (Figures 3B–E and S26). These structural properties of the thiophene-embedded polymer-like SEI were demonstrated by the correlation between the orbital composition analysis of DFT calculation and Kelvin probe force microscopy (KPFM) (Figure S27). The thiophene-embedded polymer-like SEI induced switchable polarity in the p_z orbital orientation, which undergoes dynamic rearrangement during Li plating/stripping (Figure 3F). The orbitals illustrated in yellow and cyan correspond to the positive and negative phases of the wave function, respectively. In the case of poly(thiophene), the distribution of p_z orbitals undergoes a distinct rearrangement during the Li plating and stripping process, indicating dynamic orbital polarization that facilitates Li$^+$ transport across the interphase.

In contrast, SEIs derived from poly(FEC) and poly(VC) consist of polymeric species aligned parallel to the Li-metal surface, which lack polarity switching during Li$^+$ migration and consequently exhibit limited ion transport efficiency (Figure S28).

The temperature-dependent charge-transfer kinetics across the SEI were evaluated using the Arrhenius equation[57–59]:

$$k = \mathrm{A}e^{\frac{-E_a}{RT}}, \tag{2}$$

where k denotes the rate constant, A is the pre-exponential factor, and E_a, R, and T represent the activation energy, gas constant, and absolute temperature, respectively. The SEI imparted by the baseline, FEC-based, and VC-based electrolytes predominantly restricted Li^+ transport, leading to elevated activation barriers and increased interfacial impedance, which collectively resulted in uneven Li plating (Figures S29–S31). That is, the inorganic SEI formed by the baseline electrolyte, characterized by high activation energy and low exchange current density, impeded Li^+ ion mobility and resulted in uneven Li plating (Figure S32). Similarly, the poly(FEC)- and poly(VC)-based SEI, which exhibited low exchange current density and high elastic modulus, restricted Li^+ ion transfer at the Li-metal anodes (Figure S33). In contrast, the thiophene-embedded polymer-like SEI facilitated efficient Li^+ transport, enhancing charge-transfer kinetics and lowering the activation energy for Li^+ migration at the Li-metal interface. This well-regulated interphases enabled uniform Li plating/stripping through the homogeneous distribution of cathodic current density.

An ideal SEI should combine high ionic conductivity with extremely low electronic conductivity in the range of 10^{-9} to 10^{-12} S cm^{-1} to effectively suppress parasitic side reactions at the Li-metal.[60] To assess the electrical properties of SEI, conductive atomic force microscopy (C-AFM) was utilized to record the current–voltage (i–V) spectra over the bias range of -2 to $+2$ V versus $\mathrm{Li/Li}^+$ (Figure S34). Except for the VC-derived polymeric SEI, which displayed a nonlinear current response through electron transport, the other SEIs comprising the baseline, FEC-based, and thiophene-based electrolytes exhibited negligible ohmic currents, confirming insulating properties. Notably, the thiophene-embedded polymer-like SEI enhanced rapid Li^+ ion conduction while preserving low electronic conductivity of 2.7 pS cm^{-1}, thereby facilitating uniform Li plating/stripping, maintaining the homogeneity of the Li-metal surface, and mitigating Li corrosion driven by electrolyte decomposition (Figure S35). Poly(thiophene)—a well-known semiconducting material—exhibits enhanced electronic conductivity when it possesses extended conjugation over more than six successive rings or undergoes p-type doping through oxidation.[61,62] However, the thiophene-embedded polymer-like SEI formed under the reductive environment of the Li-metal surface underwent radical coupling reactions that primarily yield short-chain oligomers, such as dimers and trimers, rather than extended polymeric networks. Hence, this oligomeric SEI exhibited intrinsically low electronic conductivity, as confirmed by the absence of ohmic current in the C-AFM measurements (Table S2). Consequently, the thiophene-embedded polymer-like SEI enhanced Li^+ mobility by generating an electron-rich microenvironment within π-conjugated C=C bonds and S atoms, while stabilizing the interfacial layer by effectively suppressing electron transfer at the Li-metal surface.

This dual functionality of the thiophene-embedded polymer-like SEI improved Li^+ charge-transfer kinetics at the interface and controlled irreversible Li^+ consumption during the Li plating/stripping across a wide current-density range of 0.667–2 mA cm^{-2} (Figures 4A–C and S36–S40). By contrast, the LiF-rich SEI formed by the baseline, FEC-based, and VC-based electrolytes lacked grain boundaries and structural irregularities that typically serve as fast-ion conduction pathways, exhibiting intrinsically low Li^+ ionic conductivity and reducing Li plating/stripping reversibility while increasing overpotential under a high current density of 2 mA cm^{-2} (Figures 4B, S19, and S38–S40).[63] Consequently, after maintaining 0 V versus $\mathrm{Li/Li}^+$ for 500 h, the precycled Li/Cu cells containing the thiophene-based electrolyte achieved superior CE (Figure S41 and Table S3). Furthermore, at increasing stripping rates, the enhanced Li^+ ion transport conferred by the thiophene-embedded polymer-like SEI minimized irreversible Li consumption compared with other electrolytes (Figures S42 and S43 and Table S4). Notably, the thiophene-embedded polymer-like SEI exhibited the lowest impedance after cell assembly in the Li/Li symmetric cell and suppressed further increase in impedance over the storage time at 25°C (Figures 4D and S44). By integrating time-dependent interfacial resistance measurements with C-AFM analysis, we quantified the ionic and electronic conductivities of the SEI (Figure S34). An ideal SEI should exhibit high Li^+ ionic conductivity (≥5 μS cm^{-1}) while maintaining ultralow electronic conductivity (<10 pS cm^{-1}) to enable efficient Li^+ transport and suppress parasitic electron-driven side reactions. Our results indicated that while the LiF-rich SEI formed by the baseline, FEC-based, and VC-based electrolytes exhibited extremely low ionic conductivities, the thiophene-embedded polymer-like SEI demonstrated ionic conductivities exceeding 5 μS cm^{-1} (Figure 4E and Table S5). Moreover, the relatively high electronic conductivity observed in the SEIs derived from FEC and VC failed to effectively block electron permeation, exacerbating side reactions and capacity degradation at elevated current densities (Figures 4A,E, S38, and S43). These findings

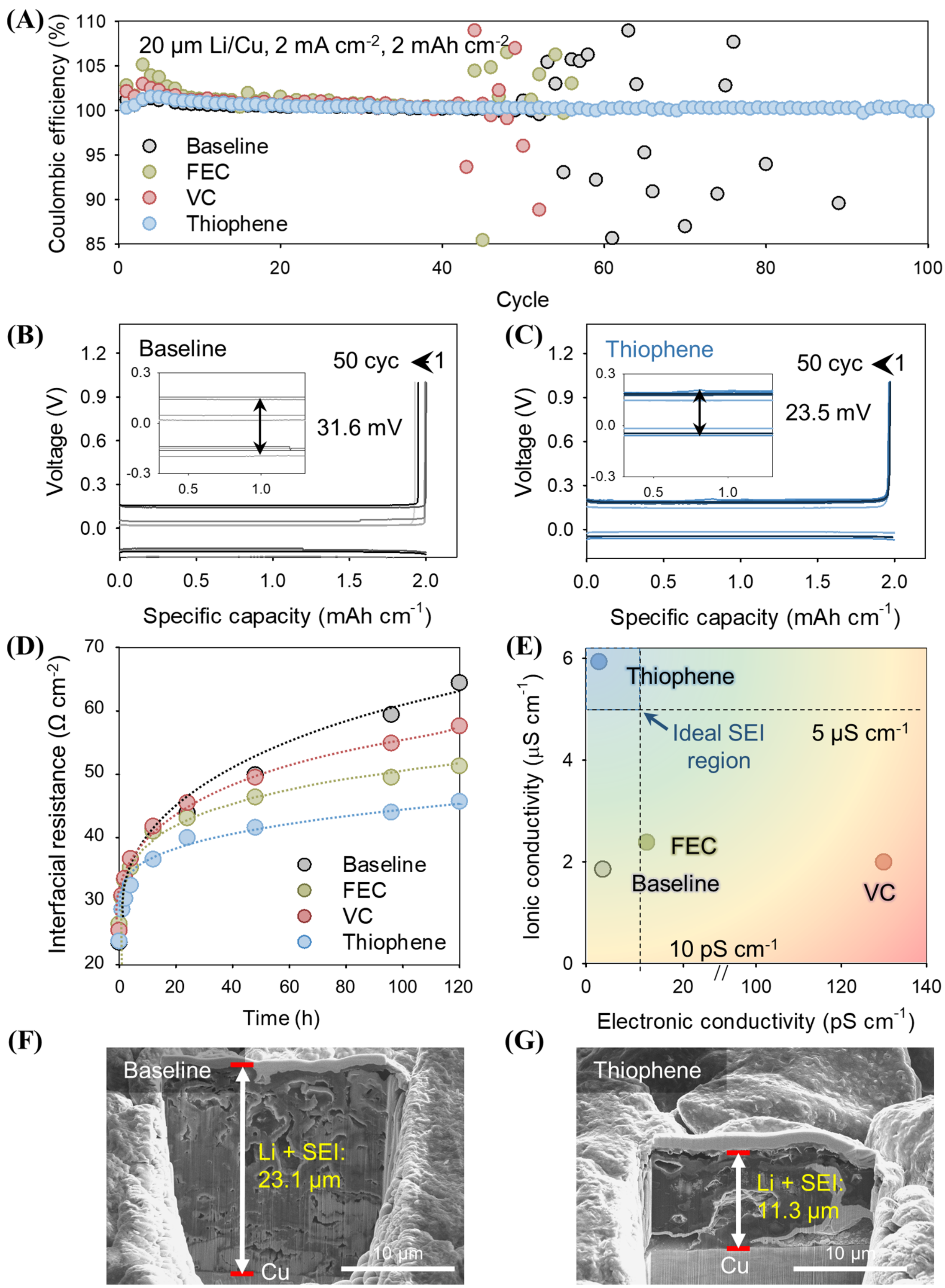

FIGURE 4 SEI stability over a wide range of current densities. (A) CE of Li/Cu cells with the baseline, FEC, VC, and thiophene electrolytes under 2 mA cm^{-2} and 2 mAh cm^{-2}. Voltage profiles of Li/Cu cells from the 1st cycle to the 50th cycle with the (B) baseline and (C) thiophene electrolytes. (D) Temporal change in the interfacial resistance of Li/Li symmetric cells with the baseline, FEC, VC, and thiophene electrolytes. The fitting curves represent a nonlinear least-squares fit to a power law ($R_{\text{Interface}} \propto at^x$). (E) Design guidelines for ideal SEIs according to ionic conductivity and electronic conductivity. The blue region enables efficient Li$^+$ transport and suppresses parasitic electron-driven side reactions. Cross-sectional SEM images of deposited Li morphology on Cu substrates extracted from Li/Cu cells with the (F) baseline and (G) thiophene electrolytes after initial Li plating at 0.2 mA cm^{-2} and 2 mAh cm^{-2}. CE, Coulombic efficiency; FEC, fluoroethylene carbonate; SEI, solid electrolyte interphase; SEM, scanning electron microscopy; VC, vinylene carbonate.

underscore the superior characteristics of the thiophene-embedded polymer-like SEI in mitigating dendritic Li growth and enhancing cycling stability at high current density. Therefore, while the SEI derived by the baseline electrolyte exhibited sluggish Li^+ ion transport, leading to non-uniform Li plating, the thiophene-embedded polymer-like SEI, with superior ionic conductivity and ultralow electronic conductivity, served as a barrier to mitigate unwanted reactions of the electrolyte with Li-metal, thereby promoting uniform Li plating (Figures 4F,G and S45).

The Li plating/stripping behavior was visualized in real time and at multiple scales using in situ electrochemical AFM (EC-AFM) and optical microscopy (OM) (Figure 5).[64–66] A Li/Li symmetric cell was utilized to monitor the surface evolution of Li-metal through topography and OM imaging during cycling (Figure 5A). At the nanoscale, AFM topography images revealed that the inorganic-rich SEI formed by the baseline electrolyte exhibited non-uniform Li behavior during cycling, with high contrast within images (Figure 5B). This resulted in a highly uneven Li-metal surface, with vertical Li growth reaching 943.5 μm (Figure 5D). Similarly, the rigid polymeric SEI generated by FEC- and VC-based electrolytes displayed heterogeneous Li growth, consistent with the behavior observed for the baseline electrolyte (Figure S46). Both electrolytes caused significant surface irregularities due to non-uniform Li plating and stripping behavior (Figure S47). By contrast, the thiophene-embedded polymer-like SEI exhibited consistent and uniform Li plating and stripping throughout the cycling process (Figure 5C). This SEI significantly suppressed vertical Li growth by enhancing the uniformity of Li plating and stripping (Figure 5E). At the microscale, OM images revealed black byproducts and small pits forming both above on the Li-metal anodes during cycling. While the baseline, FEC-based, and VC-based electrolytes led to substantial black byproduct accumulation floating above the surface, the thiophene-embedded polymer-like SEI effectively mitigated byproduct formation from electrolyte decomposition at the Li-metal, maintaining a cleaner and more uniform surface (Figure S48).

Collectively, although direct experimental observation of orbital-level polarity switching remains challenging owing to the nanoscale and ultrafast nature of orbital polarization, the mechanism was substantiated by multiple macroscopic interfacial properties that corresponded closely to the trends predicted by DFT simulations (Table S6). By broadening the interpretation beyond a simple increase in ionic conductivity, this work established an electronic-structure-driven rationale for the superior interfacial regulation afforded by the thiophene-embedded polymer-like SEI and underscored the essential role of conjugated, polarity-adaptive architectures in enabling fast and stable Li-metal cycling.

2.3 | Facile Li^+ ion transport through the thiophene-derived CEI on NCM90 cathode

Thiophene, characterized by a higher highest occupied molecular orbital (HOMO) energy level than FEC and VC, preferentially underwent oxidative decomposition, facilitating the creation of a polymer-like CEI on the NCM90 cathode (Figures 2B, S20, and S49). The thiophene-derived polymer-like CEI effectively modulated LiFSI and FSA solvent decomposition at the cathode, thereby suppressing the formation of high-resistance LiF-based CEI and predominantly producing an electron-rich S-based CEI. Dual AC resonance tracking electrochemical strain microscopy (DART ESM) and an advanced AFM-based technique were used to quantitatively compare the Li^+ ion dynamics of the thiophene-derived polymer-like CEI (Figure 6A).[67,68] ESM measured the surface strain induced by ion flux in response to an applied AC voltage through a nanoscale probe, enabling indirect assessment of ion mobility and the number of ions contributing to the observed deformation (Figure S50). Accurate frequency imaging, related to the contact resonance frequency of the probe, ensured consistent contact between the probe and sample, enhancing the quality of DART ESM measurements. To evaluate Li^+ ion dynamics within the CEI layer, the NCM90 cathodes extracted from precycled Li/NCM90 full cells were analyzed. The x-ray diffraction (XRD) profiles of the NCM90 cathodes were examined to assess the Li^+ ion concentration within the CEI layer. In the literature, shifts in the XRD peak of (113) have been established as a reliable indicator of Li^+ concentration because they are monotonic to the Li^+ concentrations.[69] The precycled NCM90 cathode using the baseline electrolyte exhibited a more pronounced (113) peak shift than the pristine cathode, indicating a higher Li^+ ion concentration at the cathode surface. By contrast, the precycled NCM90 cathode treated with the thiophene-based electrolyte displayed a less significant peak shift, reflecting a lower Li^+ ion concentration at the surface (Figure S51). The baseline electrolyte formed a thick and resistive CEI layer that obscured the electrical connection between cathode particles and grain boundaries in the ESM amplitude images (Figure 6A). Conversely, the thiophene-derived polymer-like CEI was uniformly distributed on the cathode particle and exhibited high ESM amplitude of 15.2 pm, indicating superior Li^+ ion response compared with that of the CEI formed by other electrolytes

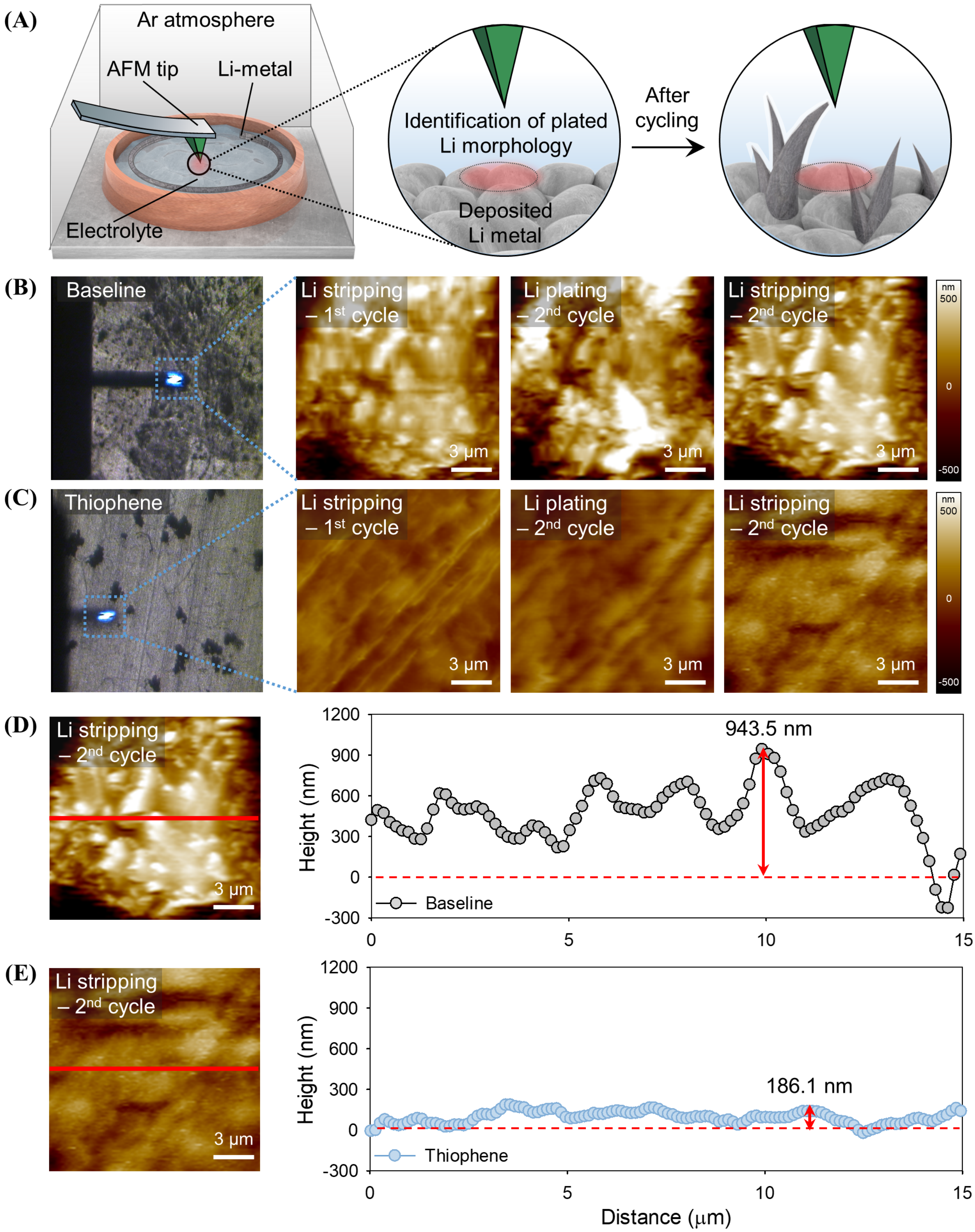

FIGURE 5 Observation of Li plating/stripping behaviors in real time. (A) Schematics of in situ AFM for observation of Li plating/stripping behavior on Li-metal anodes. In situ OM images and topography of Li-metal anodes in the (B) baseline and (C) thiophene electrolytes during cycling in Li/Li symmetric cells at 2 mA cm^{-2} and 0.25 mAh cm^{-2}. Topography images were obtained between plating/stripping. The line profiles corresponding to the red line of Li plating on the Li-metal anodes in Li/Li symmetric cells with the (D) baseline and (E) thiophene electrolytes after three cycles. AFM, atomic force microscopy; OM, optical microscopy.

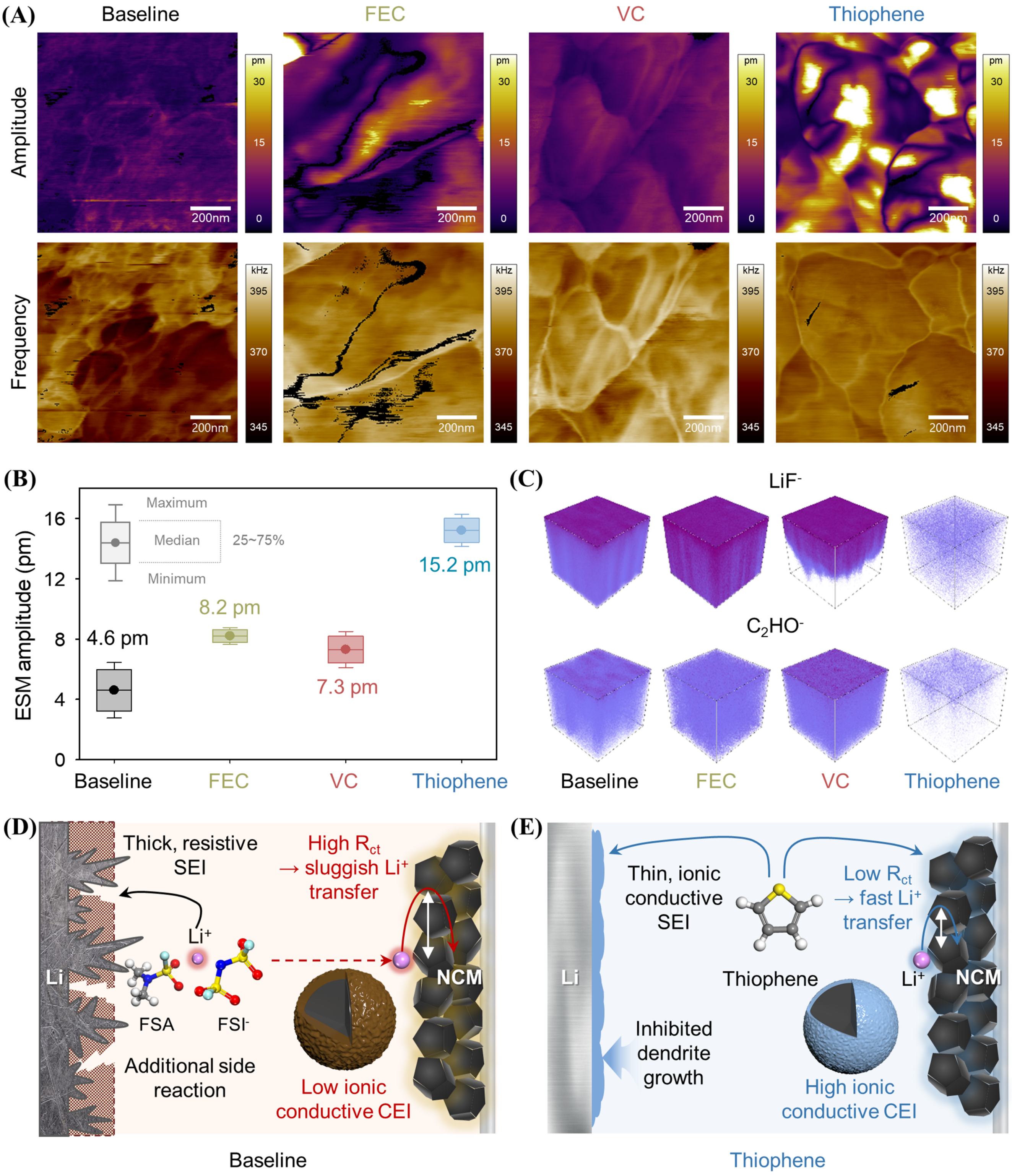

FIGURE 6 Interfacial properties of NCM90 cathodes in Li/NCM90 full cells. (A) ESM amplitude and resonance frequency for mapping Li^+ ion diffusion on NCM90 cathodes retrieved from Li/NCM90 full cells with the baseline, FEC, VC, and thiophene electrolytes after precycling. (B) Average ESM amplitude of NCM90 cathodes extracted from Li/NCM90 full cells with the aforementioned electrolytes. (C) TOF-SIMS 3D rendering images with LiF^- and C_2HO^- negative secondary ions on NCM90 cathodes extracted from Li/NCM90 full cells after precycling. Disparity in electrochemical behavior of the (D) baseline and (E) thiophene electrolytes in Li/NCM90 full cells. FEC, fluoroethylene carbonate; TOF-SIMS, time-of-flight secondary ion mass spectrometry; VC, vinylene carbonate.

(Figure 6A,B). This finding suggests that the thiophene-derived polymer-like CEI displayed enhanced ionic conductivity. TOF-SIMS 3D imaging further revealed that the CEI formed by the baseline, FEC-based, and VC-based electrolytes comprised mainly resistive LiF, attributed to LiFSI salt decomposition at the NCM90 cathode (Figures 6C and S52). By contrast, the thiophene-derived polymer-like CEI demonstrated a more favorable composition and structure, supporting improved Li^+ ion transfer. Moreover, the incorporation of conjugated C═C bonds within the CEI on the NCM90 cathodes created an electron-rich microenvironment that stabilized the interface by suppressing oxidative electrolyte decomposition during the charging process. This significantly suppressed the formation of byproducts such as C_2HO^-, which are typically generated through oxidative electrolyte decomposition (Figures 6C and S53). Interfacial analyses of precycled NCM90 cathodes demonstrated that the S-based CEI formed in the thiophene-based electrolyte exhibited superior ionic conductivity, attributed to the unshared electron pairs of S atoms. These electron pairs provided conduction pathways that facilitated Li^+ ion mobility across the CEI, thereby reducing the interfacial resistance (Figure S54). Meanwhile, the baseline electrolyte formed a resistive CEI composed of LiFSI and FSA decomposition products, leading to persistent side reactions and impeding Li^+ ion transport across the CEI (Figure 6D). The narrow energy bandgap of thiophene enabled the construction of protective interfacial layers on both Li-metal and NCM90 cathodes. The thiophene-embedded polymer-like SEI and S-enriched CEI exhibited exceptional Li^+ transport characteristics, collectively enhancing the interfacial stability and enabling efficient Li^+ ion transfer through improved charge-transfer kinetics in LMBs (Figure 6E).

2.4 | Cycling stability of LMBs under lean electrolyte and high current density

FEC, VC, and thiophene additives significantly contributed to the stabilization of Li-metal interfaces, thereby improving the cycling stability of LMBs under a low C-rate of C/3 (Figure S55). Among these, thiophene exhibited the most pronounced enhancement in cell performance. Furthermore, the Li/NCM90 stacked pouch cells incorporating the thiophene-based electrolyte were designed under lean-electrolyte condition of 2.1 g Ah^{-1}, achieving high cell capacity of 1.04 Ah while maintaining excellent cycling durability with an exceptionally high average CE of 99.94% (Figure 7A). The thiophene-based electrolyte also provided superior fast-charging capabilities compared with those of other electrolytes, which is attributed to the formation of interfacial layers with improved Li^+ ion transport properties on both the Li-metal and NCM90 cathode (Figure S56). Scanning electron microscopy (SEM) and energy-dispersive x-ray spectroscopy analyses of the surfaces of NCM90 cathodes retrieved from Li/NCM90 full cells after fast-charging evaluations revealed pronounced intensities of the F, S, and N signals for the baseline, FEC-based, and VC-based electrolytes. This finding suggested significant byproduct accumulation resulting from the decomposition of LiFSI and FSA solvents at the NCM90 cathode (Figure S57). Moreover, the uneven coverage of byproducts on the NCM90 cathode led to the formation of microcracks, compromising their structural integrity and disrupting uniform charge transport. By contrast, the thiophene-derived CEI effectively enabled the uniform coverage of the cathode particle surface, minimized electrolyte decomposition, and substantially reduced byproduct formation on the NCM90 particle compared with other electrolytes. Consequently, when the cycling C-rate of Li/NCM90 full cells was increased from C/3 to 1 C, the thiophene-based electrolyte demonstrated enhanced discharge capacity and stable CE over 150 cycles, highlighting its exceptional cycling stability (Figures S55 and S58). In comparison, the FEC-based electrolyte exhibited rapid capacity fading of the Li/NCM90 full cells at 1 C, displaying performance comparable to that of the baseline. Although VC extended the lifespan of LMBs relative to that of FEC, it exhibited severe CE fluctuations and overcharging behavior, disrupting cycling consistency and hastening the decline in cycle stability. Conversely, the thiophene-based electrolyte significantly enhanced the high-rate cycling performance of Li/NCM90 full cells at 2 C, delivering a relatively high initial cycle capacity of 187.3 mAh g^{-1} and stable operation without CE fluctuations (Figure 7B; Figures S59 and S60). As the areal capacity of the cathodes increases, impedance regulation becomes crucial owing to the extended electron pathways within the cathode and the necessity of ensuring efficient charge transfer at the cathode–electrolyte interface.[70,71] In this context, the sacrificial decomposition of the thiophene additive facilitated the creation of a stable and conductive CEI, enabling efficient high-rate cycling at cathode areal capacity of 4.1 mAh cm^{-2} under a lean-electrolyte condition with 1.5 g Ah^{-1}. Additionally, it served as a physical barrier, suppressing unwanted reactions of the electrolyte with the cathode. On the other hand, the FEC and VC-based electrolytes demonstrated cycle degradation similar to that of the baseline. This degradation is attributed to restricted Li^+ ion mobility within the spatially dense and rigid SEI structures, which led to increased overpotential at elevated C-rates (Figure S60B,C). Conversely, the thiophene-embedded polymer-like

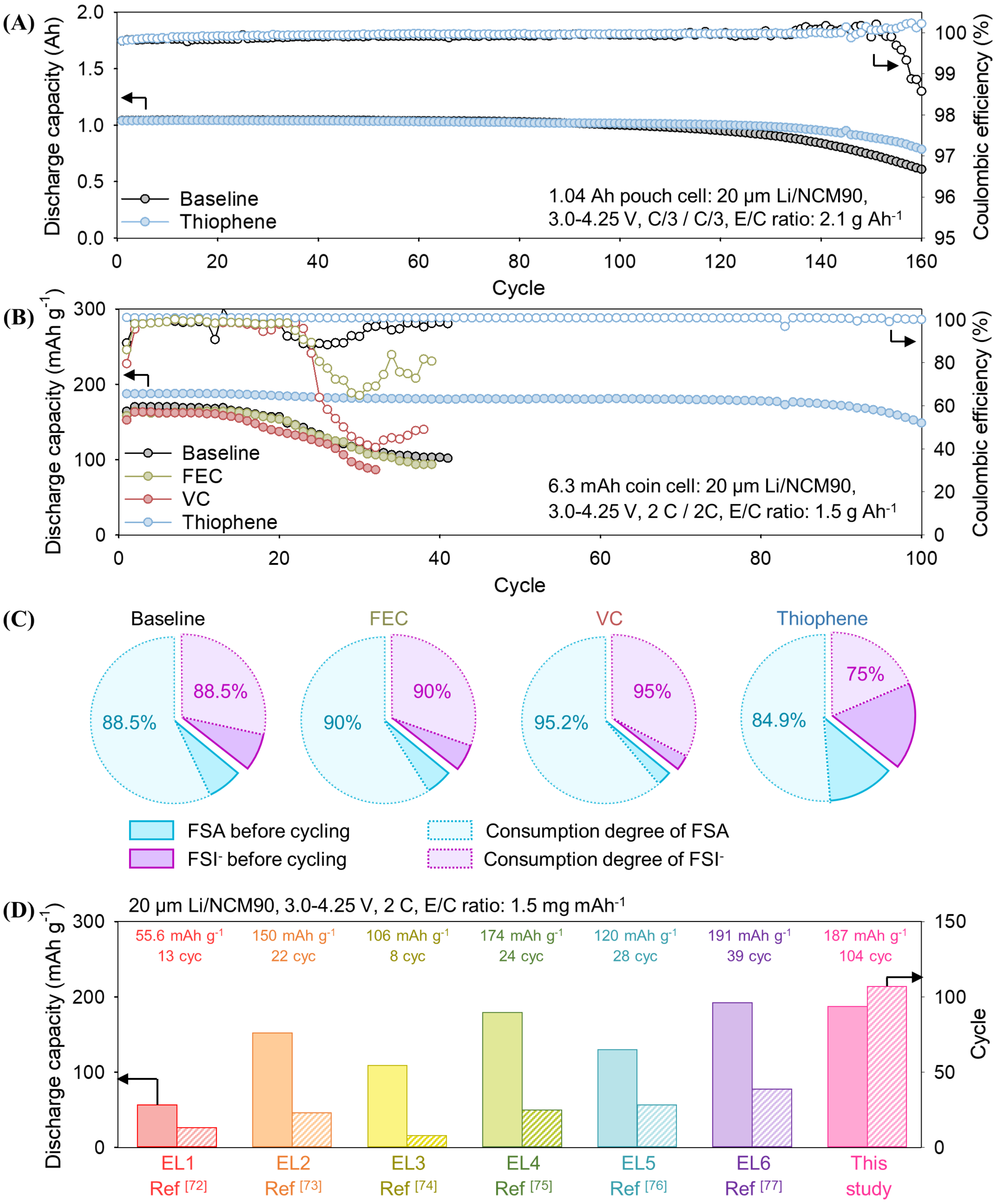

FIGURE 7 Fast-cycling capability of Li/NCM90 full cells with different electrolytes. (A) Cycle stability of Li/NCM90 pouch cells with the baseline and thiophene electrolytes. The Li/NCM90 pouch cell exhibits a capacity of 1.04 Ah and an energy density of 910 Wh L^{-1}. (B) Cycle stability of Li/NCM90 coin cells with the baseline, FEC, VC, and thiophene-based electrolytes. The cells with 4.1-mAh^{-2} cm areal capacity of the NCM90 cathode were cycled at 2 C and 25°C. (C) Comparison of the degree of electrolyte component consumption after 100 cycles measured using ^{13}C and ^{19}F NMR analysis, normalized using an internal reference of C_6F_6. (D) Comparison of cycle stability of Li/NCM90 full cells with the thiophene and the state-of-the-art electrolytes under the same cycling conditions: 4 M LiFSI DEE is labeled EL1 (1 M $LiPF_6$ + 0.1 M LiDFBP), FEC/EMC (3/7, w%) is labeled EL2, 1 M $LiPF_6$ EC/DEC + 0.5% $Sn(TOf)_2$ + 5% $LiNO_3$ is labeled EL3, 1 M $LiPF_6$ EC/DMC + 5% FEC + 0.1 M $LiNO_3$ + 0.02 M PyF is labeled EL4, 1.1 M LiFSI DME/TTE (3/2, v%) + 0.5% PTB is labeled EL5, and 2 M LiFSI BFE is labeled EL6.[72–77] FEC, fluoroethylene carbonate; LiFSI, lithium bis(fluorosulfonyl)imide; NMR, nuclear magnetic resonance; VC, vinylene carbonate; LiDFBP, lithium difluoro(bisoxalato) phosphate; EMC, ethyl methyl carbonate; EC/DEC, ethylene carbonate/diethyl carbonate; DME/TTE, 1,2-dimethoxyethane/1,1,2,2-tetrafluoroethyl-2,2,3,3tetrafluoropropyl ether; PTB, potassium trifluoro(trifluoromethyl)borate; BFE, bis(2-fluoroethyl) ether.

interfacial layer, composed of electron-rich S and conjugated C═C bonds, was constructed on both electrodes via the sacrificial decomposition of thiophene, thereby enhancing interfacial Li^+ transport kinetics. The unique structural characteristics of the thiophene-embedded polymer-like SEI, which provided effective paths for the movement of Li^+ ions and electrons, mitigated the overpotential during 2 C cycling (Figure S60D). Consequently, the thiophene-derived polymer-like interfacial layers on both electrodes significantly suppressed side reactions between the electrolyte and electrode, minimizing the consumption of LiFSI salt and FSA solvent

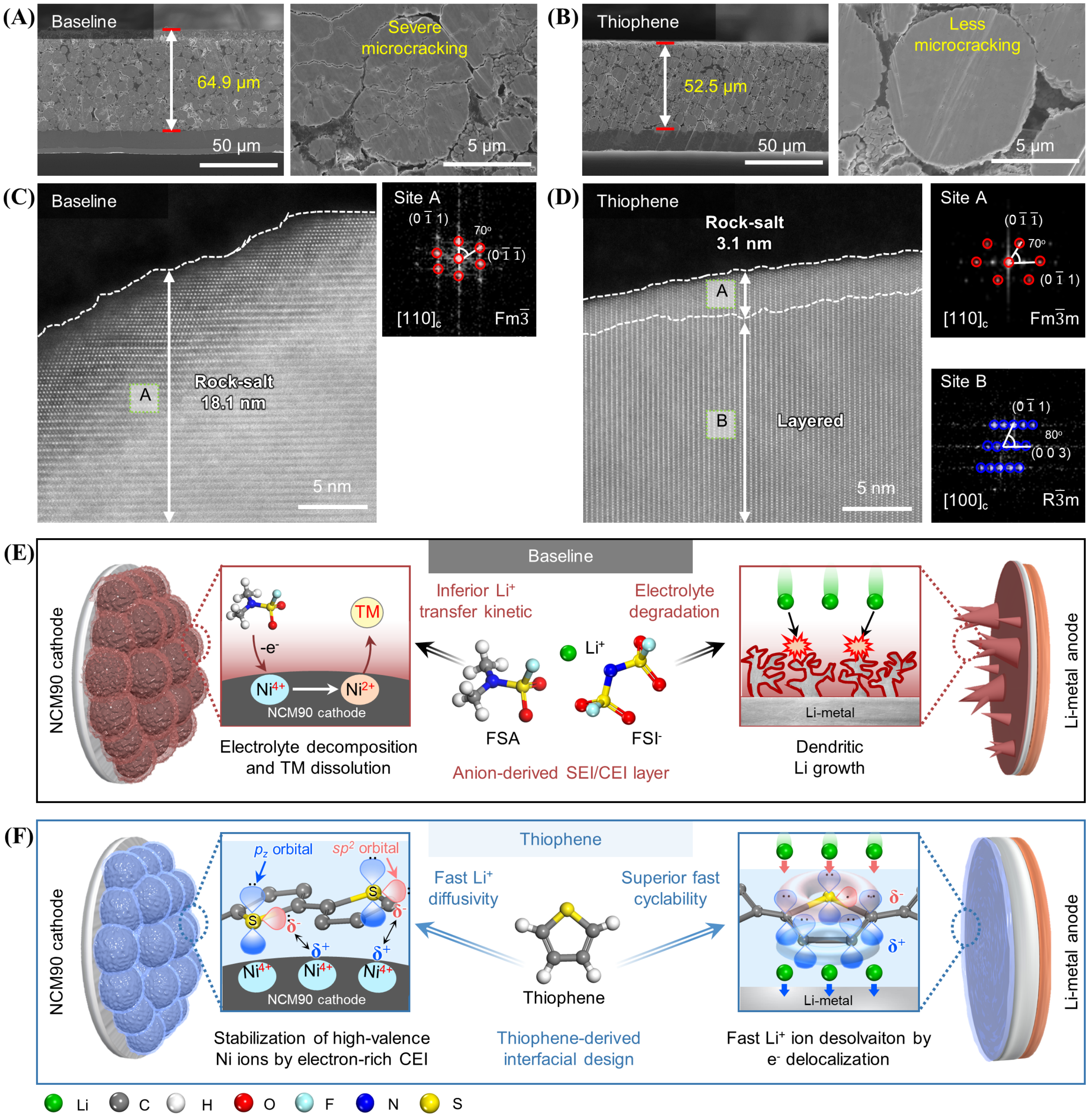

FIGURE 8 Morphological and structural stability of fast-cycled NCM90 cathodes. Cross-sectional SEM images of NCM90 cathodes retrieved from the Li/NCM90 full cells with the (A) baseline and (B) thiophene electrolytes after 100 cycles at 2 C and 25°C. Scanning transmission electron microscopy (STEM) images with fast Fourier transform (FFT) patterns of NCM90 cathodes retrieved from the Li/NCM90 full cells with the (C) baseline and (D) thiophene electrolytes after 100 cycles at 2 C and 25°C. Electrochemical behaviors of the (E) baseline and (F) thiophene electrolytes at the electrode–electrolyte interfaces during charging. SEM, scanning electron microscopy.

during fast cycling (Figures 7C and S61 and Table S7). To address the charge-transfer resistance caused by extended electronic pathways, which can function as critical internal resistance within the NCM90 cathode with high areal capacity, fast cycling of LMBs with NCM811 cathodes with lower areal capacity of 2.6 mAh cm^{-2} was evaluated (Figures S62 and S63). The baseline, FEC-based, and VC-based electrolytes, which exhibited sluggish Li^+ ion insertion and extraction, caused significant voltage hysteresis in Li/NCM811 full cells under 3 C and 5 C. Conversely, the thiophene-containing electrolyte controlled the increase in voltage hysteresis during cycling by creating an ionic-conductive CEI that enhanced the kinetics of Li^+ transport. This confirmed that the optimized interfacial design using the thiophene additive achieved remarkable cycling stability, outperforming literature-reported electrolytes in enabling fast cycling in LMBs under the same conditions employed in our evaluation (Figures 7D and S64).[72–77] Additionally, to distinguish the effect of the thiophene-driven SEI, lithium nitrate, lithium difluoro(bisoxalato) phosphate, and lithium difluorophosphate—reported as the additives to form a highly ionic conductive SEI—were incorporated into the baseline electrolyte for comparison of the fast-cycling capability in Li/NCM90 full cells (Figure S65). As a result, Li/NCM90 full cells containing these additives exhibited rapid capacity decay, indicating that fast-rate stability cannot be achieved solely by increasing the ionic conductivity of the SEI. The thiophene-based electrolyte formed a conjugation-mediated interphase that enhanced Li^+ mobility at both electrodes and delivered stable cycling performance across Ni-rich layered oxides, lithium iron phosphate, and lithium cobalt oxide cathodes, demonstrating its broad applicability for diverse LMB chemistries (Figures S66–S68). As expected, the thiophene-embedded polymer-like SEI displayed excellent fast-cycling characteristics, effectively alleviating Li-metal consumption and minimizing byproduct formation resulting from the unwanted reactions with the electrolyte at the Li metal (Figure S69). In addition, the thiophene-derived polymer-like CEI helped maintain the morphological stability of the NCM90 cathode particles without severe microcracking and thickening of the cathode during long-term cycling (Figure 8A,B). By promoting uniform Li^+ ion transfer across the thiophene-derived CEI, the structural stability of cycled NCM90 cathodes was enhanced, mitigating cathode structural degradation and the subsequent elution of transition-metal ions (Figures S70 and S71 and Table S8). These effects are attributed to two key structural features of the thiophene-derived polymer-like CEI on NCM90 cathodes. First, the incorporation of conjugated C═C bonds established an electron-rich microenvironment at the cathode surface, which mitigated oxidative electrolyte decomposition and suppressed the reduction of high-oxidation Ni ions (Ni^{4+} and Ni^{3+}) to Ni^{2+}. Second, the electron-rich S moieties within the CEI maintained interfacial charge neutrality during charging, further limiting the formation of Ni^{2+}. Because the accumulation of Ni^{2+} can promote cation mixing and trigger irreversible phase transition, it is critical for preserving the structural and electrochemical integrity of Ni-rich cathodes in LMBs. Consequently, the thiophene-derived polymer-like CEI enabled the preservation of the microstructures in the NCM90 cathode by suppressing the irreversible phase transition from layered to rock-salt during the rapid cycling of the full cell (Figures 8C,D and S72). Through the electrochemical sacrificial decomposition of the thiophene additive, well-designed interfacial layers on both electrodes in Li/NCM90 full cells enhanced the kinetics of Li^+ ion charge transfer and achieved stable cycling of LMBs under a wide range of cycling C-rates (Figure 8E,F). These findings provide valuable insights into optimizing SEI structures using electrolyte additives to significantly improve the fast-charging capabilities of LMBs.

3 | CONCLUSION

Designing optimal interfacial layers using a thiophene additive in a concentrated, fluorinated electrolyte system (3 M LiFSI FSA + 1 wt.% thiophene) enabled the rapid cycling of high-energy Li/NCM90 full cells while conserving the structural integrity of electrodes. Strong evidence was obtained for the construction of thiophene-embedded interfacial layers that ensured excellent kinetics of interfacial Li^+ ion transfer at interfaces across a wide range of cycling C-rates and conserved high-oxidation Ni ions in the NCM90 cathode with high areal-capacity via charge neutralization of electron-rich S in the CEI at highly delithiated states. Furthermore, the thiophene-embedded polymer-like SEI features unique architecture in which conjugated π systems involving sp^2 hybridized C═C frameworks generate an electron-rich microenvironment, and polarity switching through p_z orbitals oriented perpendicular to the SEI promotes a uniform Li^+ plating/stripping process. The conjugation-mediated and polarity-switchable SEI generates an electron-rich microenvironment, enabling stable electrochemical performance across a wide range of current densities. These interfacial structural characteristics achieve long-life performance and stability of LMBs by suppressing problems such as the side reaction with the electrolyte, electrolyte depletion, dead Li formation, and degradation of both Li-metal and cathode interfaces. Consequently, electrolyte additive technology that regulates the interfacial structures can be integrated with various electrolyte systems, and the interfacial architecture demonstrated here offers a viable pathway for electrolyte design platforms that enable the rapid cycling of LMBs. This study establishes a new paradigm in orbital-engineered interfacial design in LMBs, bridging molecular-scale electronic polarization with macroscopic fast-charging stability.

4 | EXPERIMENTAL SECTION

4.1 | Preparation of electrolyte and electrode

Three moles of LiFSI (≥99.7%, Chunbo Fine Chemicals Co., Ltd.) was dissolved in FSA (≥99.95%, Enchem) to produce the baseline electrolyte, to which 1 wt.% FEC (battery-grade >99.9%, Enchem), VC (battery-grade >99.9%, Enchem), or thiophene (>99%, Sigma-Aldrich) was subsequently added for comparative analysis of the fast-cycling capability. After overnight stirring to ensure complete dissociation of the 3 M LiFSI salt, calcium hydride (CaH_2, 95%, Sigma-Aldrich) was added to remove moisture from the electrolytes. The reaction between CaH_2 and moisture produced $Ca(OH)_2$, which was subsequently filtered out. All electrolyte fabrication processes were conducted in a glove box filled with Ar gas (concentrations of O_2 and H_2O: <1 ppm).

The cathode slurry was composed of 96 wt.% NCM90 as the active material, 2 wt.% carbon black, and 2 wt.% poly(vinylidene fluoride) binder. These materials were fully dispersed in *N*-methylpyrrolidone (Aladdin) and then coated onto Al foil. Prior to electrochemical measurements, the NCM90 cathode (thickness: 68.7 μm, loading level: 20.1 mg cm^{-2}, areal capacity: 4.1 mAh cm^{-2}) was dried in a vacuum oven at 110°C for 10 h. The 20-μm-thick Li-metal anode was obtained from Honjo. For LMBs with 2032 coin-type cells, 10 μL of electrolyte was used, corresponding to an E/C ratio of 1.5 g Ah^{-1}. For the 1.04 Ah pouch cell, the electrolyte amount was controlled at 2.1 g Ah^{-1}, enabling evaluation under practical lean-electrolyte conditions.

A number of 2032 coin-type Li/graphite half-cells were assembled to evaluate the stability of the SEI layer formed on Li-metal. The graphite consisted of 97.3 wt.% graphite active material, 2.2 wt.% binder (1.3 wt.% styrene-butadiene rubber and 0.9 wt.% sodium carboxymethyl cellulose), and 0.5 wt.% Denka Black. The electrodes exhibited a thickness of 132.0 μm and a mass loading of 20.76 mg cm^{-2}.

4.2 | Electrochemical measurements

All cell fabrication processes were conducted in a glove box filled with Ar gas (concentrations of O_2 and H_2O: <1 ppm). The interfacial characteristics of the electrolytes were examined utilizing Li/Li symmetric cells and Li/Cu cells with 2016 coin-type configurations. Prior to measuring the activation energy for Li^+ ion transfer at the Li-metal/electrolyte interfaces, the Li/Li symmetric cells were precycled at 0.2 mA cm^{-2} and 2 mAh cm^{-2} (WBCS3000, WonATech). The activation energy was measured over the wide temperature range of 25–55°C. The exchange current density was determined using cyclic voltammetry over the potential range of −0.2 to 0.2 V versus Li/Li^+ (VSP-2e, BioLogic). The time dependence of the interfacial resistance was evaluated immediately after assembling the Li/Li symmetric cells with the different electrolytes. The interfacial resistance was extracted by fitting the semicircle region of the Nyquist plots. The fitting curves were generated using a nonlinear least-squares fit of a power law ($R_{\text{Interface}} \propto at^x$).[78–80] Based on Ohm's law ($V = IR$), the ionic conductivity of the SEI was calculated from the fitted interfacial resistance values. Li/Cu cells were precycled at 0.2 mA cm^{-2} and 2 mAh cm^{-2} to develop an SEI on the Li metal. Subsequently, the normalized Li-corrosion current was evaluated by depositing Li metal on the Cu substrate and holding at 0 V versus Li/Li^+ for 50 h. Li plating/stripping behavior was subsequently observed via cycle performance tests at various current densities ranging between 0.667 and 2 mA cm^{-2}, maintaining a fixed areal capacity of 2 mAh cm^{-2}. The CE of the Li/Cu cells was measured by gradually increasing the current density for Li stripping from 0.2 to 2 mA cm^{-2}, while Li was plated onto the Cu substrate at 0.2 mA cm^{-2}. Before electrochemical evaluation, the Li/NCM90 full cells in 2032 coin-type configurations were twice precycled between 3.0 and 4.25 V versus Li/Li^+ at 25°C. Leakage-current measurements were conducted on Li/NCM90 full cells by maintaining the fully charged cells at 4.25 V versus Li/Li^+ for 10 h. For rate-capability assessments, Li/NCM90 full cells were discharged at C/3 while the charging rate was sequentially increased from C/3 to C/2, 1 C, 2 C, 3 C, 5 C, and 10 C. The last three cycles were returned to C/3 to examine the recovery performance of the LMBs. To assess fast-cycling stability, Li/NCM90 full cells with different electrolytes were cycled at a high current density of 8.2 mA cm^{-2}.

4.3 | Characterization

All analyses were performed in a glove box filled with Ar gas (concentrations of O_2 and H_2O: <1 ppm). To examine the interfacial characteristics, the cells were dismantled, and the electrodes were washed with DME to eliminate residual electrolyte. A focused ion beam (FIB) (Helios Nanolab 450, FEI) was utilized to examine the morphologies of deposited Li on the Cu substrate. Topography, KPFM, in situ EC-AFM, and nanoindentation measurements were performed using an MFP-3D Origin AFM instrument (Oxford Instruments Asylum Research Inc.) equipped with an electrochemical closed cell (EC-cell). The other measurements were performed using an electrical closed cell. Both cell types were assembled inside a glove box, transferred to outside of the glove box, and then integrated with the AFM head. All EC-cell measurements were conducted in a liquid electrolyte, while the electrical closed-cell measurements were performed in an inert Ar environment (99.9999% purity). Additionally, ESM measurements were performed using a Cypher-ES AFM (Oxford Instruments Asylum Research Inc.). Pt/Ir-coated tips (Electrostatic force microscopy, resonance frequency 75 kHz, NanoWorld) were used for KPFM and ESM measurements. KPFM measurements on samples comprising SEI layers formed by the baseline electrolyte and thiophene additive were conducted using the same AFM tip to ensure consistent results. Surface potentials were quantitatively compared using the reference work function of the tip, based on Equation (3):

$$\phi_{\text{sample}} = \phi_{\text{tip}} - V_{\text{CPD}} \cdot e, \tag{3}$$

where ϕ_{sample} represents the sample work function, ϕ_{tip} represents the tip work function, and e represents the electronic charge.[81–85] The DART mode was utilized for ESM measurements, with an electrical-tuning step conducted prior to measurement. The peak width was maintained at 15 kHz, the drive frequency of the vertical signal was approximately five times the resonance frequency, and the drive amplitude was set to 5 V to ensure a stable resonance peak. A simple harmonic oscillator calculation was performed following the measurements to calibrate the amplified amplitude. Diamond-like C-coated tips (a resonance frequency of 13 kHz, BudgetSensors) were used for the in situ EC-AFM experiments. A Li/Li symmetric cell was assembled in the glove box and then connected to a galvanostat (Zive SP1, WonATech) and the AFM head under ambient conditions. Galvanostatic charge/discharge was performed under a 2-mA cm^{-2} current density and 0.25-mAh cm^{-2} capacity. Upon completion of each stripping and plating step, cycling was paused, and the AFM tip was carefully engaged with the electrode surface. Topography imaging was then conducted over a 20 μm × 20 μm area to minimize stage drift and crop the image of the same region. After image acquisition, the tip was retracted from the surface to prevent interference during subsequent cycling. The focus of the optical microscope was then adjusted to the Li-metal surface to record morphological changes during operation. The tip position was delicately adjusted throughout the measurement to ensure imaging of the same region. OM images were captured every 30 s after setting the focus on the surface before cycling. Diamond-coated tips (resonance frequency 400 kHz, Nanosensors) were used for nanoindentation measurements. The inverse optical-lever sensitivity was calibrated to approximately 140–150 nm V^{-1}, and the spring constant was set to 110–120 N m^{-1}. Each sample was subjected to a loading force of 5 μN. To estimate the elastic modulus of the SEI layers while minimizing the influence of underlying Li, the initial 20% of the force–displacement curve was fitted using the Hertzian model provided by Asylum Research software. SEM (SU8230, Hitachi) was conducted under ultrahigh vacuum to examine the morphologies of the Li-metal anodes and the structural degradation of NCM90 cathodes in Li/NCM90 full cells after cycling. TOF-SIMS measurements were performed using a TOF-SIMS 5 instrument (ION-TOF GmbH, Germany) to determine the oligomeric structure of SEI on Li-metal anodes and compare the compositions of the CEI layers on the NCM90 cathodes after precycling in Li/NCM90 full cells with different electrolytes. A Bi_3^{++} primary ion beam (1.3 pA, 1000 keV) was employed for surface analysis, while a 2-keV Cs^+ secondary ion beam was used for sputtering in the negative-ion detection mode. The FSI^- anion and FSA solvent consumption in the electrolytes during the cycling of Li/NCM90 full cells was analyzed using ^{19}F nuclear magnetic resonance (NMR) spectroscopy (AVIIIHD, 500 MHz, Bruker). The NMR spectra were referenced to 1 wt.% hexafluorobenzene (C_6F_6) (>99.95%, Sigma-Aldrich) in tetrahydrofuran-d8 (99.5%, NMR grade, Eurisotop, Saint Aubin, France). Scanning transmission electron microscopy (STEM, Spectra Ultra, Thermo Fisher) with a high resolution of 200 kV was performed to compare the structural stability of the NMC90 cathodes in Li/NCM90 full cells with the baseline and thiophene electrolytes after 100 cycles. Before STEM, the NCM90 cathode surfaces were coated with a C layer using an FIB system.

DFT Calculations: The Dmol^3 program was used for DFT calculations to evaluate the HOMO and lowest unoccupied molecular orbital (LUMO) levels of LiFSI, FSA, and the additives, along with the formation and adsorption energies.[86,87] The Becke three-parameter hybrid functional integrated with the Lee–Yang–Parr correlational functional was utilized to derive the exchange–correlation energy.[88] Spin-polarized and Van Der Waals corrections were calculated via the Tkatchenko–Scheffler method.[89] All relativistic core treatments and a double numerical plus polarization 4.4 basis set were utilized to explain the atomic orbital basis set and core electrons, respectively. The convergence criterion was set to 1×10^{-6} Ha for self-consistent calculation. The convergence criteria were fixed to 1×10^{-5} Ha, 0.002 Ha Å^{-1}, and 0.005 Å to maximize the energy change, force, and displacement, respectively. To precisely simulate the experimental conditions, the conductor-like screening model was utilized as an implicit solvent effect. To accurately capture the solvent screening effects of the electrolyte, the dielectric constant of FSA (i.e., 52.46) was utilized.[90,91]

The thiophene radical-thiophene radical formation energies ($\Delta E_{\mathrm{Formation}}$) were calculated using the equation:

$$\Delta E_{\mathrm{Formation}} = E_{\mathrm{total}} - 2E_{\mathrm{Thiophene}} + (1/2)\, nE_{\mathrm{H2}}, \tag{4}$$

where E_{total} represents the total energy of the product, $E_{\mathrm{Thiophene}}$ represents the total energy of thiophene, and E_{H2} represents the total energy of H_2 gas. The adsorption energy ($\Delta E_{\mathrm{Adsorption}}$) between the Li atoms and electrolyte (i.e., poly(FEC), poly(VC), and poly(thiophene)) was calculated using the equation:

$$\Delta E_{\mathrm{Adsorption}} = E_{\mathrm{total}} - \left(E_{\mathrm{Li}} + E_{\mathrm{electrolyte}}\right), \tag{5}$$

where E_{total} represents the total energy of the product, E_{Li} represents the total energy of the Li atom, and $E_{\mathrm{electrolyte}}$ represents the total energy of the electrolytes of poly(FEC), poly(VC), and poly(thiophene), respectively.

To investigate orbital polarization, we considered three interface materials (i.e., poly(FEC), poly(VC), and poly(thiophene)) for the plating and stripping processes and constructed six model systems. In each system, Li metal was replaced with a thermodynamically stable Li_7 cluster,[92] and each electrolyte was modeled as trans-type dimers—a choice guided by experimental TOF-SIMS analysis and confirmed to be thermodynamically favorable by DFT calculations (Figure 2D). A system consisting of a molecule Li cluster and dimer was placed in a box with dimensions of 30 × 30 × 30 Å^3.

The orbital contributions of the proposed models were evaluated through maximally localized Wannier functions (MLWFs).[90,91] The Wannier functions are essentially the Fourier transform of the Bloch function and can be considered as a localized bond/atomic-like version of the Bloch waves. They explicitly provide a direct, real-space picture of bonding, σ/π, lone pairs, and d-orbital without breaking the periodicity. The DFT calculations were performed with the Vienna Ab initio Simulation Package,[93,94] incorporating the Perdew–Burke–Ernzerhof[95] functional within the generalized gradient approximation as the exchange-correlation functional. The electron–ion interaction was described by the projector-augmented wave method.[96] The electronic wavefunctions were expanded using an energy cutoff 560 eV, with 1 × 1 × 1 Gamma-centered k-point sampling of the Brillouin zone for the system under large vacuum. The developed structures were optimized by relaxing all atomic positions and constants until the residual forces and energy difference fell below 0.01 eV Å^{-1} and 10^{-6} eV, respectively.

AUTHOR CONTRIBUTIONS

J.-A.L., H.K., Y.C., and S.H.K. contributed equally to this work. E.K., S.S., K.H.R., and N.-S.C. proposed and designed the projects. J.-A.L. and H.K. conceptualized the original draft and conducted characterizations and electrochemical measurements. Y.C., S.K., and S.H. performed various AFM analyses for mapping Li$^+$ ion diffusion on the interfacial layer and observation of Li plating/stripping behavior. R.K.V. assisted with data analysis and interpretation of AFM data. S.H.K., S.A.U.H., and S.K.K. executed the DFT calculations. J.-A. L., H.K., Y.C., S.H.K., S.K., S.A.U.H., M.S., S.K., R K.V., S.K.K., S.H., and N.-S.C. wrote the manuscript. All authors analyzed the data and contributed to the discussion.

ACKNOWLEDGMENTS

This research was supported by the Hyundai Motor Company and a National Research Foundation of Korea (NRF) grant funded by the Korean government (MSIT) (RS-2025-00554246). It was partially supported by the Korea Institute of Energy Technology Evaluation and Planning (KETEP) and the Ministry of Trade, Industry & Energy (MOTIE) of the Republic of Korea (RS-2024-00402410). A portion of the data analysis was supported by the Center for Nanophase Materials Sciences, which is a US Department of Energy, Office of Science User Facility at Oak Ridge National Laboratory. Computational resources were supported from UNIST High Performance Computing (HPC) systems and Korea Institute of Science and Technology Information (KSC-2023-CRE-0143).

CONFLICT OF INTEREST STATEMENT

The authors declare no conflicts of interest.

DATA AVAILABILITY STATEMENT

The data that support the findings of this study are available from the corresponding author upon reasonable request.

ORCID

Seungbum Hong https://orcid.org/0000-0002-2667-1983
Nam-Soon Choi https://orcid.org/0000-0003-1183-5735

REFERENCES

1. Liu B, Zhang J-G, Xu W. Advancing lithium metal batteries. *Joule*. 2018;2(5):833-845.
2. Zhang R, Li NW, Cheng XB, Yin YX, Zhang Q, Guo YG. Energy storage: advanced micro/nanostructures for lithium metal anodes. *Adv Sci*. 2017;4(3):1600445.
3. Zhang Y, Zuo T-T, Popovic J, et al. Towards better Li metal anodes: challenges and strategies. *Mater Today*. 2020;33:56-74.
4. Li S, Jiang M, Xie Y, Xu H, Jia J, Li J. Developing high-performance lithium metal anode in liquid electrolytes: challenges and progress. *Adv Mater*. 2018;30(17):1706375.
5. Cheng X-B, Zhang R, Zhao C-Z, Zhang Q. Toward safe lithium metal anode in rechargeable batteries: a review. *Chem Rev*. 2017;117(15):10403.
6. Guo Y, Li H, Zhai T. Reviving lithium-metal anodes for next-generation high-energy batteries. *Adv Mater*. 2017;29(29):1700007.
7. Wu H, Jia H, Wang C, Zhang JG, Xu W. Recent progress in understanding solid electrolyte interphase on lithium metal anodes. *Adv Energy Mater*. 2021;11:2003092.
8. Shan X, Zhong Y, Zhang L, et al. A brief review on solid electrolyte interphase composition characterization technology for lithium metal batteries: challenges and perspectives. *J Phys Chem C*. 2021;125(35):19060-19080.
9. Xu Y, Dong K, Jie Y, et al. Promoting mechanistic understanding of lithium deposition and solid-electrolyte interphase (SEI) formation using advanced characterization and simulation methods: recent progress, limitations, and future perspectives. *Adv Energy Mater*. 2022;12(19):2200398.
10. Cao W, Li Q, Yu X, Li H. Controlling Li deposition below the interface. *eScience*. 2022;2(1):47-78.
11. Yasin G, Arif M, Mehtab T, et al. Understanding and suppression strategies toward stable Li metal anode for safe lithium batteries. *Energy Storage Mater*. 2020;25:644.
12. Wang Z, Sun Z, Li J, et al. Insights into the deposition chemistry of Li ions in nonaqueous electrolyte for stable Li anodes. *Chem Soc Rev*. 2021;50(5):3178.
13. Hao F, Verma A, Mukherjee PP. Mechanistic insight into dendrite–SEI interactions for lithium metal electrodes. *J Mater Chem A*. 2018;6(40):19664-19671.
14. Fang R, Li Y-X, Wang W-W, Gu Y, Mao B-W. Kinetic understanding of lithium metal electrodeposition for lithium anodes. *Phys Chem Chem Phys*. 2024;26(36):23544.
15. Choi N-S, Lee YM, Park JH, Park J-K. Interfacial enhancement between lithium electrode and polymer electrolytes. *J Power Sources*. 2003;119:610-616.
16. Lee JA, Kim S, Cho Y, et al. Compositionally sequenced interfacial layers for high-energy Li-metal batteries. *Adv Sci*. 2024;11(17):2310094.
17. Gao X, Zhou Y-N, Han D, et al. Thermodynamic understanding of li-dendrite formation. *Joule*. 2020;4(9):1864-1879.
18. Aslam MK, Niu Y, Hussain T, et al. How to avoid dendrite formation in metal batteries: innovative strategies for dendrite suppression. *Nano Energy*. 2021;86:106142.
19. Wang C, Wang A, Ren L, et al. Controlling Li ion flux through materials innovation for dendrite-free lithium metal anodes. *Adv Funct Mater*. 2019;29(49):1905940.
20. Han F, Westover AS, Yue J, et al. High electronic conductivity as the origin of lithium dendrite formation within solid electrolytes. *Nat Energy*. 2019;4(3):187-196.
21. Zhang Q-K, Zhang X-Q, Wan J, et al. Homogeneous and mechanically stable solid–electrolyte interphase enabled by trioxane-modulated electrolytes for lithium metal batteries. *Nat Energy*. 2023;8(7):725.
22. Park HE, Hong CH, Yoon WY. The effect of internal resistance on dendritic growth on lithium metal electrodes in the lithium secondary batteries. *J Power Sources*. 2008;178(2):765-768.
23. Jana A, Woo SI, Vikrant K, García RE. Electrochemomechanics of lithium dendrite growth. *Energ Environ Sci*. 2019;12(12):3595-3607.
24. Bai P, Li J, Brushett FR, Bazant MZ. Transition of lithium growth mechanisms in liquid electrolytes. *Energ Environ Sci*. 2016;9(10):3221-3229.
25. Zhang R, Cheng XB, Zhao CZ, et al. Conductive nanostructured scaffolds render low local current density to inhibit lithium dendrite growth. *Adv Mater*. 2016;28(11):2155-2162.
26. Zhang S, Li R, Hu N, et al. Tackling realistic Li+ flux for high-energy lithium metal batteries. *Nat Commun*. 2022;13(1):5431.
27. Chen C, Liang Q, Wang G, Liu D, Xiong X. Grain-boundary-rich artificial SEI layer for high-rate lithium metal anodes. *Adv Funct Mater*. 2022;32(4):2107249.
28. Wu F, Yuan Y-X, Cheng X-B, et al. Perspectives for restraining harsh lithium dendrite growth: towards robust lithium metal anodes. *Energy Storage Mater*. 2018;15:148-170.
29. Kim S, Lee J-A, Lee TK, et al. Wide-temperature-range operation of lithium-metal batteries using partially and weakly solvating liquid electrolytes. *Energ Environ Sci*. 2023;16(11):5108-5122.
30. Kim S, Lee TK, Kwak SK, Choi N-S. Solid electrolyte interphase layers by using lithiophilic and electrochemically active ionic additives for lithium metal anodes. *ACS Energy Lett*. 2021;7(1):67-69.
31. Chen H, Pei A, Lin D, et al. Uniform high ionic conducting lithium sulfide protection layer for stable lithium metal anode. *Adv Energy Mater*. 2019;9(22):1900858.
32. Zhang S-J, Yin Z-W, Wu Z-Y, et al. Achievement of high-cyclability and high-voltage Li-metal batteries by heterogeneous SEI film with internal ionic conductivity/external electronic insulativity hybrid structure. *Energy Storage Mater*. 2021;40:337-346.
33. Gao S, Sun F, Liu N, Yang H, Cao P-F. Ionic conductive polymers as artificial solid electrolyte interphase films in Li metal batteries – a review. *Mater Today*. 2020;40:140-159.
34. Liu Y, Lin D, Yuen PY, et al. An artificial solid electrolyte interphase with high Li-ion conductivity, mechanical strength, and flexibility for stable lithium metal anodes. *Adv Mater*. 2016;29(10):1605531.
35. Lee J-A, Kang H, Kim S, et al. Unveiling degradation mechanisms of anode-free Li-metal batteries. *Energy Storage Mater*. 2024;73:103826.
36. Choi N-S, Lee YM, Seol W, Lee JA, Park J-K. Protective coating of lithium metal electrode for interfacial enhancement with gel polymer electrolyte. *Solid State Ion*. 2004;172(1-4):19-24.

37. Nishi Y. The development of lithium ion secondary batteries. *Chem Record*. 2001;1(5):406-413.
38. Kim S, Park G, Lee SJ, et al. Lithium-metal batteries: from fundamental research to industrialization. *Adv Mater*. 2023;35(43):2206625.
39. Lee J, Jeong SH, Nam JS, et al. Toward thin and stable anodes for practical lithium metal batteries: a review, strategies, and perspectives. *EcoMat*. 2023;5(12):e12416.
40. Li Z, Zheng Y, Liao C, et al. Advanced polymer materials for protecting lithium metal anodes of liquid-state and solid-state lithium batteries. *Adv Funct Mater*. 2024;34(42):2404427.
41. Chae B-J, Park JH, Song HJ, et al. Thiophene-initiated polymeric artificial cathode-electrolyte interface for Ni-rich cathode material. *Electrochim Acta*. 2018;290:465-473.
42. Lin X, Chen Y, Fu Y, et al. Fluorinated thiophene-based electrolyte additives enable a robust cathode electrolyte interphase with conformal homogeneity for a high-voltage $LiNi_{0.8}Co_{0.15}Al_{0.05}O_2$ cathode. *J Phys Chem C*. 2024;128(12):4988-4996.
43. Ren W, Huang Y, Li S, et al. 3-Thiopheneboronic acid: an effective additive for regulation on electrode/electrolyte interphase of lithium metal battery with high-loading cathode. *Electrochim Acta*. 2021;386:138485.
44. Li S, Tang R, Hu C, Niu X, Wang L. Graphdiyne-loaded polycaprolactone nanofiber scaffold for peripheral nerve regeneration. *J Colloid Interface Sci*. 2023;646:150-412.
45. He Y, Zhang Y, Yu P, et al. Ion association tailoring SEI composition for Li metal anode protection. *J Energy Chem*. 2020;45:1.
46. Wan S, Song K, Chen J, et al. Reductive competition effect-derived solid electrolyte interphase with evenly scattered inorganics enabling ultrahigh rate and long-life span sodium metal batteries. *J Am Chem Soc*. 2023;145(39):21661-21671.
47. Wang Z, Wang Y, Zhang Z, et al. Building artificial solid-electrolyte interphase with uniform intermolecular ionic bonds toward dendrite-free lithium metal anodes. *Adv Funct Mater*. 2020;30(30):2002414.
48. Wen K, Tan X, Chen T, Chen S, Zhang S. Fast Li-ion transport and uniform Li-ion flux enabled by a double-layered polymer electrolyte for high performance Li metal battery. *Energy Storage Mater*. 2020;32:55-64.
49. Hagopian A, Doublet M-L, Filhol J-S. Thermodynamic origin of dendrite growth in metal anode batteries. *Energ Environ Sci*. 2020;13(12):5186-5197.
50. Xue W, Shi Z, Huang M, et al. FSI-inspired solvent and “full fluorosulfonyl” electrolyte for 4 V class lithium-metal batteries. *Energ Environ Sci*. 2020;13(1):212-220.
51. Dato MA, Edgington J, Hung C, et al. Sulfur solutions: advancing high voltage and high energy lithium batteries with organosulfur electrolytes. *Adv Energy Mater*. 2024;14(13):2303794.
52. Xue W, Huang M, Li Y, et al. Ultra-high-voltage Ni-rich layered cathodes in practical Li metal batteries enabled by a sulfonamide-based electrolyte. *Nat Energy*. 2021;6(5):495.
53. Yi A, Mamaeva N, Li H, Spudich JL, Rothschild KJ. Resonance Raman study of an anion channelrhodopsin: effects of mutations near the retinylidene Schiff Base. *Biochemistry*. 2016;55(16):2371-2380.
54. Smith SO, Braiman MS, Myers AB, et al. Vibrational analysis of the all-trans-retinal chromophore in light-adapted bacteriorhodopsin. *J Am Chem Soc*. 1987;109(10):3108-3125.
55. Smith SO, Hornung I, Van Der Steen R, et al. Are C14-C15 single bond isomerizations of the retinal chromophore involved in the proton-pumping mechanism of bacteriorhodopsin? *Proc Natl Acad Sci USA*. 1986;83(4):967.
56. Smith SO, Pardoen JA, Lugtenburg J, Mathies RA. Vibrational analysis of the 13-cis-retinal chromophore in dark-adapted bacteriorhodopsin. *J Phys Chem*. 1987;91(4):804-819.
57. Dong L, Yan HJ, Liu QX, et al. Quantification of charge transport and mass deprivation in solid electrolyte interphase for kinetically-stable low-temperature lithium-ion batteries. *Angew Chem Int Ed*. 2024;136:e202411029.
58. Zabara MA, Katırcı G k, ÜlgÜt B. Operando investigations of the interfacial electrochemical kinetics of metallic lithium anodes via temperature-dependent electrochemical impedance spectroscopy. *J Phys Chem C*. 2022;126(27):10968.
59. Churikov A. Transfer mechanism in solid-electrolyte layers on lithium: influence of temperature and polarization. *Electrochim Acta*. 2001;46(15):2415.
60. Xu K. Electrolytes and interphases in Li-ion batteries and beyond. *Chem Rev*. 2014;114(23):11503.
61. Yamamoto T. Molecular assembly and properties of polythiophenes. *NPG Asia Mater*. 2010;2(2):54.
62. Furukawa Y, Akimoto M, Harada I. Vibrational key bands and electrical conductivity of polythiophene. *Synth Met*. 1987;18(1-3):151.
63. Guo R, Gallant BM. Li_2O solid electrolyte interphase: probing transport properties at the chemical potential of lithium. *Chem Mater*. 2020;32(13):5525.
64. Wang S, Liu D, Cai X, et al. Promoting the reversibility of lithium ion/lithium metal hybrid graphite anode by regulating solid electrolyte interface. *Nano Energy*. 2021;90:106510.
65. Zhang Z, Said S, Smith K, et al. Characterizing batteries by in situ electrochemical atomic force microscopy: a critical review. *Adv Energy Mater*. 2021;11(38):2101518.
66. Um JH, Yu SH. Lithium metal batteries: unraveling the mechanisms of lithium metal plating/stripping via in situ/operando analytical techniques. *Adv Energy Mater*. 2021;11(27):2003004.
67. Balke N, Jesse S, Morozovska A, et al. Nanoscale mapping of ion diffusion in a lithium-ion battery cathode. *Nat Nanotechnol*. 2010;5(10):749-754.
68. Joo S, Jeong U, Gong C, Hong S. Bridging mechanical and electrical analyses in AFM: advances, techniques, and applications. *Acc Mater Res*. 2024;6(1):17-27.
69. Kitada K, Murayama H, Fukuda K, et al. Factors determining the packing-limitation of active materials in the composite electrode of lithium-ion batteries. *J Power Sources*. 2016;301:11-17.
70. Kim Y, Kim M, Lee T, et al. Investigation of mass loading of cathode materials for high energy lithium-ion batteries. *Electrochem Commun*. 2023;147:107437.
71. Wu F, Liu M, Li Y, et al. High-mass-loading electrodes for advanced secondary batteries and supercapacitors. *Electrochem Energ Rev*. 2021;4(2):382.
72. Chen Y, Yu Z, Rudnicki P, et al. Steric effect tuned ion solvation enabling stable cycling of high-voltage lithium metal battery. *J Am Chem Soc*. 2021;143(44):18703.
73. Shi P, Liu F, Feng Y, Zhou J, Rui X, Yu Y. The synergetic effect of lithium bisoxalatodifluorophosphate and fluoroethylene carbonate on dendrite suppression for fast charging lithium metal batteries. *Small*. 2020;16(30):2001989.

74. Zhang W, Wu Q, Huang J, et al. Colossal granular lithium deposits enabled by the grain-coarsening effect for high-efficiency lithium metal full batteries. *Adv Mater*. 2020;32(24):2001740.
75. Fang W, Wen Z, Chen L, et al. Constructing inorganic-rich solid electrolyte interphase via abundant anionic solvation sheath in commercial carbonate electrolytes. *Nano Energy*. 2022;104:107881.
76. Xia M, Jiao T, Liu G, et al. Rational design of electrolyte solvation structure for stable cycling and fast charging lithium metal batteries. *J Power Sources*. 2022;548:232106.
77. Zhang G, Chang J, Wang L, et al. A monofluoride ether-based electrolyte solution for fast-charging and low-temperature non-aqueous lithium metal batteries. *Nat Commun*. 2023;14(1):1081.
78. Boyle DT, Huang W, Wang H, et al. Corrosion of lithium metal anodes during calendar ageing and its microscopic origins. *Nat Energy*. 2021;6(5):487-494.
79. Kwon H, Kim H, Hwang J, et al. Borate–pyran lean electrolyte-based Li-metal batteries with minimal Li corrosion. *Nat Energy*. 2024;9(1):57-69.
80. Zaban A, Zinigrad E, Aurbach D. Impedance spectroscopy of Li electrodes. 4. A general simple model of the Li−solution interphase in polar aprotic systems. *J Phys Chem*. 1996;100(8):3089.
81. Melitz W, Shen J, Kummel AC, Lee S. Kelvin probe force microscopy and its application. *Surf Sci Rep*. 2011;66(1):1-27.
82. Park G, Moon H, Shin S, et al. Spatially uniform lithiation enabled by single-walled carbon nanotubes. *ACS Energy Lett*. 2023;8(7):3154.
83. Wang W-W, Gu Y, Yan H, et al. Evaluating solid-electrolyte interphases for lithium and lithium-free anodes from nanoindentation features. *Chem*. 2020;6(10):2728-2745.
84. Tan YH, Liu Z, Zheng JH, et al. Inorganic composition modulation of solid electrolyte interphase for fast charging lithium metal batteries. *Adv Mater*. 2024;36(30):2404815.
85. Villeneuve-Faure C, Boudou L, Makasheva K, Teyssedre G. Methodology for extraction of space charge density profiles at nanoscale from Kelvin probe force microscopy measurements. *Nanotechnology*. 2017;28(50):505701.
86. Delley B. DMol, a standard tool for density functional calculations: review and advances. *Theor Comput Chem*. 1995;2:221-254.
87. Delley B. An all-electron numerical method for solving the local density functional for polyatomic molecules. *J Chem Phys*. 1990;92(1):508.
88. Stephens PJ, Devlin FJ, Chabalowski CF, Frisch MJ. Ab initio calculation of vibrational absorption and circular dichroism spectra using density functional force fields. *J Phys Chem*. 1994;98(45):11623.
89. Tkatchenko A, Scheffler M. Accurate molecular van der Waals interactions from ground-state electron density and free-atom reference data. *Phys Rev Lett*. 2009;102(7):073005.
90. Marzari N, Mostofi AA, Yates JR, Souza I, Vanderbilt D. Maximally localized Wannier functions: theory and applications. *Rev Mod Phys*. 2012;84(4):1419-1475.
91. Mostofi AA, Yates JR, Pizzi G, et al. An updated version of wannier90: a tool for obtaining maximally-localised Wannier functions. *Comput Phys Commun*. 2014;185(8):2309-2310.
92. Hai-Rong M, Ping L, Qing-Quan G, Hui-Li L. Formation mechanism and binding energy for body-centred regular octahedral structure of Li_7 cluster. *Commun Theor Phys*. 2007;48(4):717-720.
93. Kresse G, Furthmüller J. Efficient iterative schemes for ab initio total-energy calculations using a plane-wave basis set. *Phys Rev B*. 1996;54(16):11169-11186.
94. Kresse G, Furthmüller J. Efficiency of ab-initio total energy calculations for metals and semiconductors using a plane-wave basis set. *Comput Mater Sci*. 1996;6(1):15-50.
95. Perdew JP, Burke K, Ernzerhof M. Generalized gradient approximation made simple. *Phys Rev Lett*. 1996;77(18):3865-3868.
96. Kresse G, Joubert D. From ultrasoft pseudopotentials to the projector augmented-wave method. *Phys Rev B*. 1999;59(3):1758-1775.

SUPPORTING INFORMATION

Additional supporting information can be found online in the Supporting Information section at the end of this article.

How to cite this article: Lee J-A, Kang H, Cho Y, et al. Conjugation-mediated and polarity-switchable interfacial layers for fast cycling of lithium-metal batteries. *InfoMat*. 2026;e70126. doi:10.1002/inf2.70126